

## RESEARCH ARTICLE

10.1002/2016JB013103

## Key Points:

- Multibeam bathymetry and geochemical surveys performed off Zannone Island provide evidence of an undocumented hydrothermal field
- Giant depressions represent the main seabed morphology related to fluid venting
- Geochemical signature of the collected fluids indicates active CO<sub>2</sub>-dominated degassing with a significant contribution of mantle volatiles

## Correspondence to:

E. Martorelli,  
eleonora.martorelli@igag.cnr.it

## Citation:

Martorelli, E., F. Italiano, M. Ingrassia, L. Macelloni, A. Bosman, A. M. Conte, S. E. Beaubien, S. Graziani, A. Sposato, and F. L. Chiocci (2016), Evidence of a shallow water submarine hydrothermal field off Zannone Island from morphological and geochemical characterization: Implications for Tyrrhenian Sea Quaternary volcanism, *J. Geophys. Res. Solid Earth*, 121, 8396–8414, doi:10.1002/2016JB013103.






Received 15 APR 2016

Accepted 20 NOV 2016

Accepted article online 22 NOV 2016

Published online 20 DEC 2016

## Evidence of a shallow water submarine hydrothermal field off Zannone Island from morphological and geochemical characterization: Implications for Tyrrhenian Sea Quaternary volcanism

E. Martorelli<sup>1</sup> , F. Italiano<sup>2</sup> , M. Ingrassia<sup>1,3</sup>, L. Macelloni<sup>1,4</sup>, A. Bosman<sup>1</sup> , A. M. Conte<sup>5</sup>, S. E. Beaubien<sup>3</sup> , S. Graziani<sup>3</sup>, A. Sposato<sup>1</sup>, and F. L. Chiocci<sup>1,3</sup> 

<sup>1</sup>CNR-IGAG, Rome, Italy, <sup>2</sup>INGV, Palermo, Italy, <sup>3</sup>Earth Science Department, Sapienza University of Rome, Rome, Italy, <sup>4</sup>NIUST, University of Mississippi, University, Mississippi, USA, <sup>5</sup>CNR-IGG, Rome, Italy

**Abstract** Discoveries from multibeam bathymetry and geochemical surveys performed off Zannone Island (western Pontine Archipelago, Tyrrhenian Sea) provide evidence of an undocumented hydrothermal field characterized by ongoing fluid emissions and morphologically complex giant depressions located in shallow water (<150 m water depth). Based on a detailed morpho-bathymetric study we identify the seabed morphologies produced by hydrothermal fluid emission activity. We recognize five giant depressions (length >250 m) that host pockmarks, mounds, small cones, and active fluid vents, which are interpreted as complex fluid-escape features developed both through vigorous-explosive events and steady seepage. Their spatial distribution suggests that the NE-SW trending faults bounding the Ponza-Zannone structural high and the shallow fractured basement are favorable conditions for the upward migration of hydrothermal fluids. Moreover, we performed a detailed geochemical study to investigate the source of the hydrothermal fluids. The geochemical signature of the collected fluids provides information of active CO<sub>2</sub>-dominated degassing with a significant contribution of mantle volatiles, with measured <sup>3</sup>He/<sup>4</sup>He values > 3.0 Ra that are similar to those recorded at Stromboli and Panarea volcanoes. The hydrothermal system produces volatiles that may originate from residual magma batches, similar to the Pleistocene trachytes cropping out in the SE sector of Ponza Island that were probably intruded in the shallow crustal levels and never erupted. The discovery of the Zannone hydrothermal field updates the record of active hydrothermal areas of the Mediterranean Sea. Moreover, the recognition of several giant hydrothermal depressions characterized by a complex morphology is peculiar for the Mediterranean Sea.

### 1. Introduction

Fluid transfer from the geosphere to the biosphere, hydrosphere, and atmosphere is a fundamental process of the Earth's material recycling. Plate boundaries, volcanic arcs, and hydrocarbon-mature continental margins are the geological environments that largely determine this transfer process, with migration occurring through many pathways at different timescales and magnitudes [Suess, 2014]. The emission of geosphere fluids is a well-known and common geological phenomena in Italy that has been reported and studied for over two centuries [Spallanzani, 1792]. The Italian peninsula, specifically the Tyrrhenian margin, resides in a very dynamic and complex geological setting, characterized by diffuse Plio-Quaternary magmatism and volcanism [Peccerillo, 2003] that is mainly associated with the back-arc extension of the Tyrrhenian region [Doglioni *et al.*, 1999; Sartori, 2003; Faccenna *et al.*, 2004]. All these processes promote heat flow anomalies and a large variety of thermal emissions [Minissale, 2004, and references therein] that are particularly widespread in the coastal zone of the Latium and Campanian regions, where Quaternary volcanoes are the dominant geological environment (Figure 1). The central Tyrrhenian margin is considered an area of medium to high enthalpy geothermal systems (heat flow values between 50 and 120 mW/m<sup>2</sup>) linked to both the Plio-Quaternary volcanic activity and a thin continental crust of <25 km [Funicello *et al.*, 1979; Della Vedova *et al.*, 1984; Cavarretta *et al.*, 1985; Minissale, 2004].

Several CO<sub>2</sub> emission sites have been detected in both onshore and offshore areas characterized by young or active volcanism; in some cases CO<sub>2</sub> emissions occur in areas without evidence of magmatic activity, such as the Apennine chain [Italiano *et al.*, 2008, and references therein]. Onshore, CO<sub>2</sub>-rich gas emissions are present

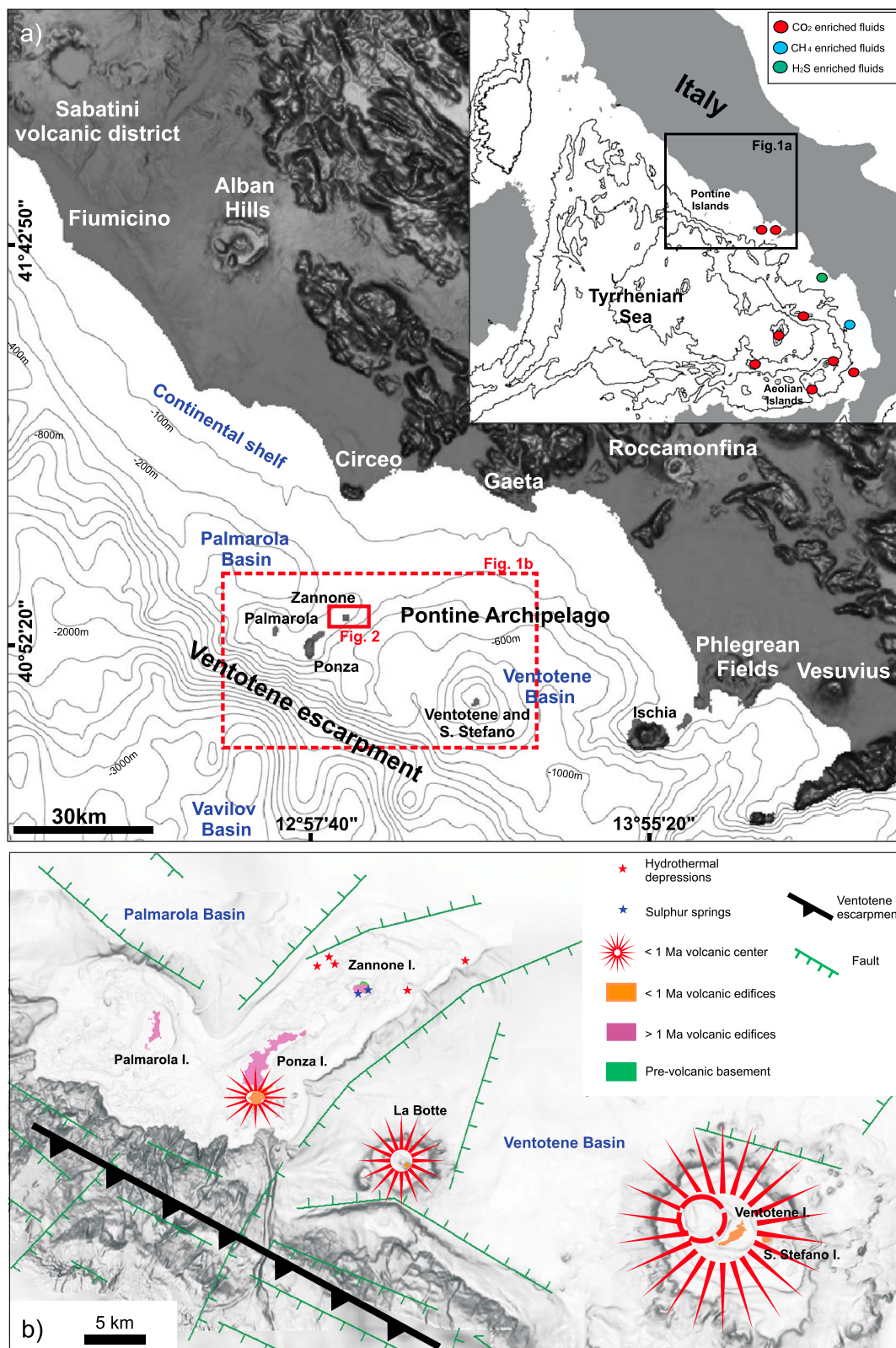


**Figure 1.** Study area and sketch of main tectonic and volcanic features. (a) Location map of the study area (bathymetric data derived from GEBCO Digital Atlas); the inset shows the location of the fluid emission sites (circles) reported in the scientific literature for the Tyrrhenian Sea (see text for details). (b) Main tectonic features and volcanic edifices of the Pontine Archipelago (see Figure 1a for location); faults were obtained from Zitellini *et al.* [1984] and De Rita *et al.* [1986]. Sulphur springs described by Tricoli [1855] and hydrothermal depressions analyzed in this study are also indicated.

**Table 1.** List of the Submarine Vents Discovered in the Tyrrhenian Sea

Site	Type of Fluids	Temperature (°C)	Depth	Geological Features	Biological Communities
Panarea Island	CO <sub>2</sub>	20–130	5–150	crater-like depression	<i>Posidonia oceanica</i> , bacterial mats
Vulcano Island	CO <sub>2</sub>	15–100	0.3–800	/	bacteria and archaea
Enarete seamount	CO <sub>2</sub>	/	400–600	caldera structure ?	fossil coral, mollusk shells
Marsili seamount	CO <sub>2</sub>	/	300–676	altered deposits	bacteria
Palinuro seamount	CO <sub>2</sub>	/	600	caldera structure	bacteria, archaea, and virus
Calabro-Tyrrhenian margin	H <sub>2</sub> S-CH <sub>4</sub> ?	14	730	mud diapirs, pockmarks, and mud volcanoes	Lucinids, crustaceans, and bacteria
Capo Vaticano	CO <sub>2</sub>	14	75–100	ridge structure	
Capo Palinuro	H <sub>2</sub> S	25	0–10	cave	bacteria and cyanobacteria
Ischia Island	CO <sub>2</sub>	60–80?	0–2		bacteria
Bay of Naples	CO <sub>2</sub>	14	71–158	flat seafloor	/

as dry springs, soil diffuse degassing, fumaroles, and vents located in pools and springs. Offshore, CO<sub>2</sub>-rich gas emissions (Table 1) are known to occur in shallow water around the Ischia Island coastal zone [Maugeri *et al.*, 2010], in the Bay of Naples [Passaro *et al.*, 2014; Passaro *et al.*, 2016], offshore Capo Vaticano [Loreto *et al.*, 2014, 2015], and throughout the Aeolian Archipelago [Italiano, 2009b; Maugeri *et al.*, 2010; Monecke *et al.*, 2012; Graziani *et al.*, 2014]. Deep-sea hydrothermal activity, highlighted by <sup>3</sup>He and dissolved CO<sub>2</sub> anomalies, is reported at almost all the Tyrrhenian seamounts [Lupton *et al.*, 2011; Walker *et al.*, 2012; Italiano *et al.*, 2014b]. H<sub>2</sub>S-rich gas emissions are also present [Stüben *et al.*, 1996; Rovere *et al.*, 2014]. In general, offshore CO<sub>2</sub> emissions are associated with the cooling of magmatic bodies.

A new and previously unknown gas venting system (the Zannone Giant Pockmark, ZGP) has been recently discovered offshore Zannone Island in the central Tyrrhenian Sea [Ingrassia *et al.*, 2015]. The ZGP is a wide and morphologically complex seafloor depression, hosting vigorous-venting activity which promotes formation of authigenic mineralization and growth of different types of bacterial mats. The ZGP lies in relatively shallow water (<150 m water depth) along a narrow insular shelf. Here venting activity has been observed in video images, fish finder sonograms, multibeam water column backscatter imagery, and remotely operated vehicle (ROV) images.

To understand the origin of the active fluid emissions, we carried out an extensive geochemical survey, including sampling of the water column by Niskin bottles and of the bubbling gases at the seafloor by ROV, as well as measurements of dissolved CO<sub>2</sub> using in situ sensors. The geochemical results are interpreted to infer the source of the fluids vented in the Zannone offshore and compared with data from other well-known Tyrrhenian hydrothermal areas (e.g., Aeolian Islands and Marsili seamount) that release fluids of volcanic and geothermal origin.

Moreover, very high resolution multibeam bathymetry of the seafloor in the vicinity of the ZGP has been analyzed to map other venting structures and to determine the extent and spatial characteristics of the degassing hydrothermal system. Different scenarios describing the origin of the hydrothermal fluids are proposed, each one having different implications for the geodynamic evolution of the Tyrrhenian Basin.

## 2. Study Area

### 2.1. The Pontine Archipelago

The Pontine Archipelago (Figures 1a and 1b) consists of five major islands divided into two groups: Ponza, Palmarola, and Zannone to the northwest and Ventotene and Santo Stefano to the southeast. The five islands are located in the central sector of the Tyrrhenian Sea, about 30 km south of the Circeo Promontory and adjacent to a wide, NW-SE trending escarpment (i.e., the Ventotene escarpment, Figure 1a).

The islands are rooted on a sedimentary basement affected by Plio-Pleistocene extensional deformations [Zitellini *et al.*, 1984; Marani *et al.*, 1986; Marani and Zitellini, 1986; De Rita *et al.*, 1986; Malinverno and Ryan, 1986]. These deformations created several morpho-structural elements, such as (1) a NW-SE trending escarpment (the Ventotene Escarpment, Figure 1a); (2) a NE-SW elongated high (the Ponza-Zannone structural high, Figures 1a and 1b) that is bounded by extensional faults affecting the Plio-Pleistocene postorogenic cover and divides two major areas of sedimentation (the Palmarola and Ventotene intraslope basins, Figures 1a

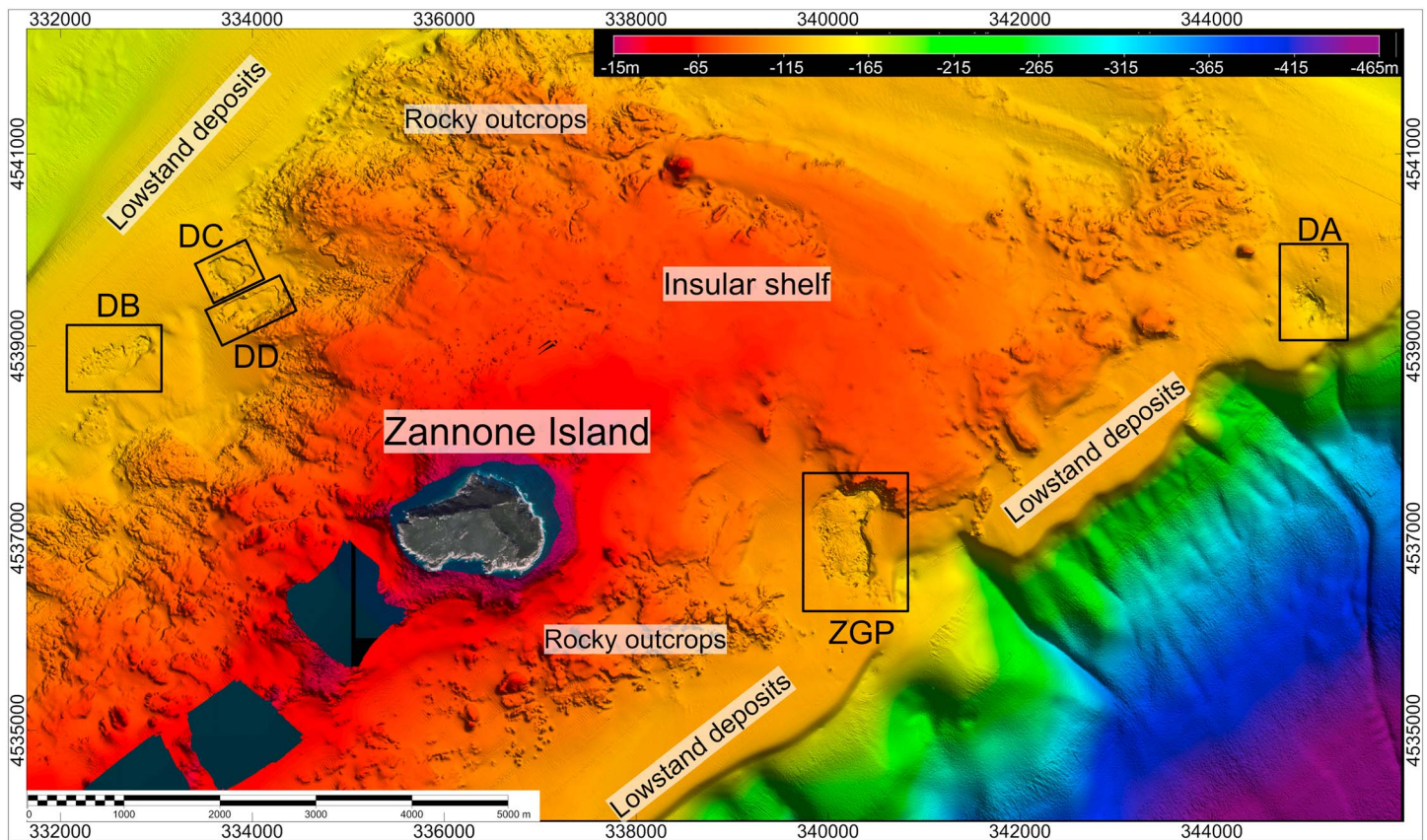


**Figure 2.** Shaded relief map of the seafloor surrounding Zannone Island (see Figure 1a for location), showing the main geomorphological features and the occurrence of five large depressions (ZGP, DA, DB, DC, and DD).

and 1b); and (3) volcanic edifices related to diffuse magmatic activity [Barberi *et al.*, 1967; Cadoux *et al.*, 2005, and references therein].

The magmatic activity developed mainly in two cycles. The first cycle occurred during the Pliocene with the emplacement of rhyolites, forming the dominant products that outcrop in the western Pontine Islands. The second cycle occurred during the Pleistocene with the emplacement of trachytes in the SE sector of Ponza Island and basalts and trachytes-phonolites at Ventotene and Santo Stefano Islands [Conte and Dolfi, 2002; Cadoux *et al.*, 2005]. At Zannone, the pre-Pliocene metamorphic and sedimentary basement rocks are exposed [De Rita *et al.*, 1986].

**2.2. The Zannone Giant Pockmark (ZGP)**

The ZGP is located in the eastern part of the Zannone insular shelf, between 85 and 125 m water depth (Figure 2). It is a well-defined morphological depression that covers an area of about 0.5 km<sup>2</sup> and is 5–18 m deep. It occurs on a gentle slope area, in correspondence with a depositional wedge (low stand deposits in Figure 2) formed by deposits emplaced during the last glacio-eustatic cycle [Ingrassia *et al.*, 2015].

The ZGP (Figures 3a and 3 of Ingrassia *et al.* [2015]) has an irregular shape, with the minimum axis of 500 m in the E-W direction and the maximum axis of 900 m in the NNW-SSE direction. It is bounded by well-defined, irregularly trending scarps that are locally subcircular to subrectilinear in shape; to the north the depression boundary is represented by a rocky escarpment. The floor of the ZGP is very irregular and characterized by several mounds, cones, pockmarks, and small ridges. These elements are dispersed throughout the depression, so that areas with a smooth and regular morphology are mostly absent. The irregular morphology of the ZGP floor and the shape of its margins suggest coalescence of 200–500 m diameter crater-like features [Ingrassia *et al.*, 2015]. The deepest crater (about 15 m deep) is located in the northern sector of the ZGP and is about 250 m wide.

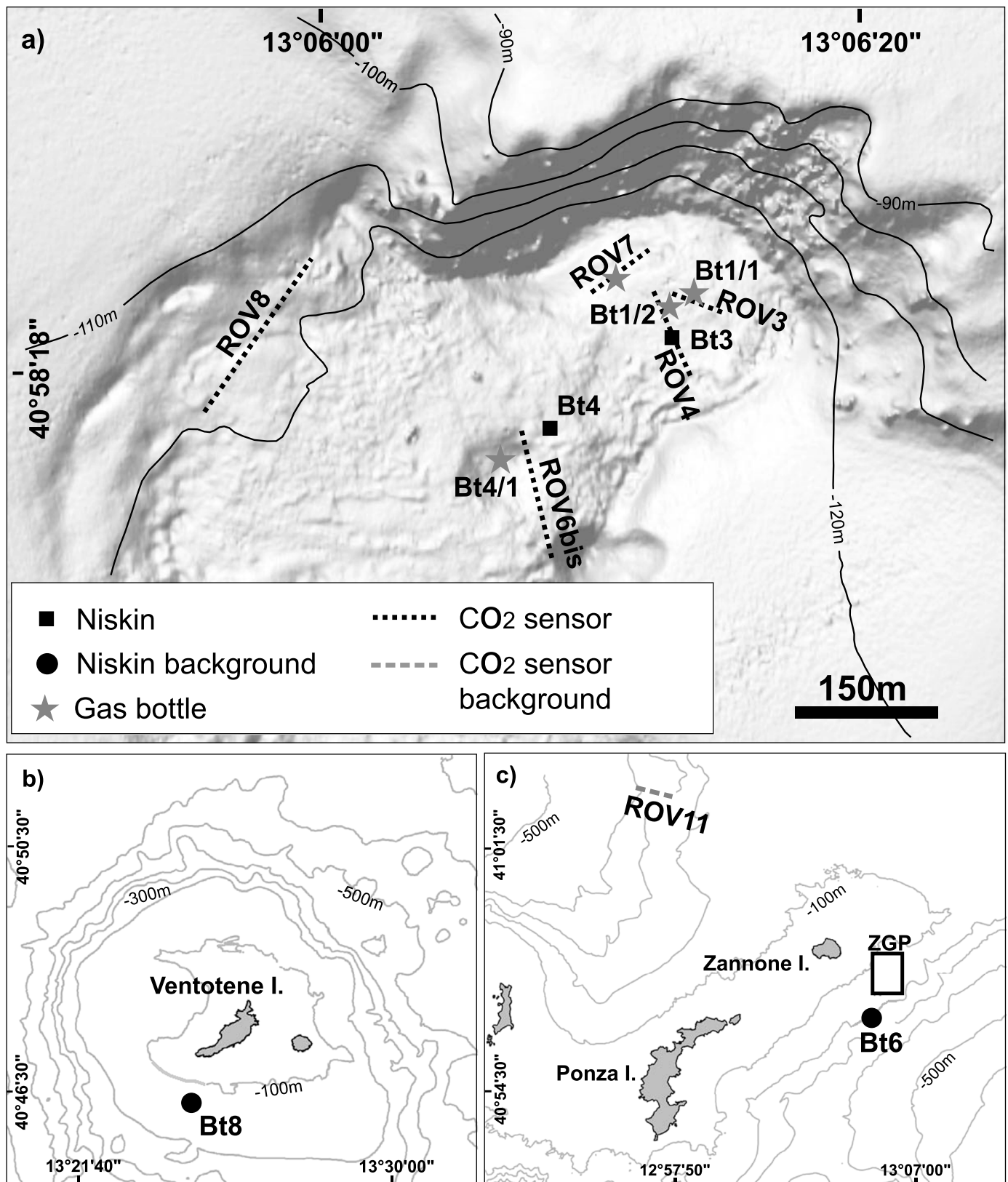


**Figure 3.** Location of sampling stations and CO<sub>2</sub> measurements: (a) High-resolution multibeam bathymetry map of the ZGP with indication of location of the water column samples, gas bubbling samples, and pCO<sub>2</sub> probe transects acquired in the northern sector of the ZGP. (b and c) Location map of the water column samples and pCO<sub>2</sub> probe transects background values, acquired away from the ZGP. A complete overview of the ZGP is given in Figure 7a.

**Table 2.** Location and Main Features of the Collected Water and Gas Samples<sup>a</sup>

Date	Sample No.	Sample ID	Cruise	East	North	Depth (m)	Area
<i>Vertical Cast (Dissolved Gases)</i>							
29/05/2014	1	BT3	Bolle 2014	340397	4537387	50	ZGP
	2					100	ZGP
	3					129 bottom	ZGP
30/05/2014	4	BT4	Bolle 2014	340293	4537299	50	ZGP
	5					100	ZGP
	6					127	ZGP
01/06/2014	7	BT6	Bolle 2014	339010	4534887	50	outside ZGP
	8					100	outside ZGP
	9					129 bottom	outside ZGP
03/06/2014	10	BT8	Bolle 2014	364772	4514499	123 bottom	SW Ventotene
<i>Bubbling Gases</i>							
29/05/2014	11	BT1/1	Bolle 2014	340395	4537414	129	ZGP
	12	BT1/2	Bolle 2014	340395	4537414	129	ZGP
30/05/2014	13	BT4/1	Bolle 2014	340263	4537276	127	ZGP
	14	BT4/2	Bolle 2014	340263	4537276	127	ZGP

<sup>a</sup>Coordinates reference system UTM WGS84 zone 33 N. Vertical casts sampling was carried out using Niskin bottles; bubbling gas sampling was performed using an ROV equipped with a manipulator. See text for details.

### 3. Material and Methods

#### 3.1. Multibeam Bathymetry

High-resolution multibeam bathymetry data were acquired using Kongsberg EM 710 (100–70 kHz) and EM 3002D (300 kHz) echo sounders, during two oceanographic cruises performed on board the R/V *Maria Grazia* and the R/V *Urania* (CNR, Italy) on November 2009 (MAGIC\_IGAG\_1009) and August 2011 (MAGIC\_IGAG\_0811), respectively. All data were georeferenced using a differential GPS and processed with dedicated software (Caris Hips and Sips 8.1.7). Bathymetric data calibration was performed by patch tests and daily sound speed profiles. High-resolution digital elevation models of the seafloor between 70 and 150 m water depth have been produced with cell sizes from 1 m to 0.5 m, covering an area of 2 km<sup>2</sup>.

#### 3.2. Geochemical Survey

An extensive geochemical survey was carried out on May 2014 (Bolle cruise) over several sites where gas bubble flares have been clearly recognized in video images, fishfinder sonograms, water column acoustic backscatter, and ROV images [see *Ingrassia et al.*, 2015]. The geochemical survey was mainly focused on the sites located in the northern sector of the ZGP (Figure 3a and Table 2) where the gas venting appeared to be more intense. Three geochemical sampling methods were employed: Niskin bottle profiles to sample the water column at venting sites, mini bottles handled by a ROV manipulator to directly collect gas bubbles at the vent mouth, and a GasPro pCO<sub>2</sub> probe mounted on the ROV frame and towed along transects over the venting sites.

##### 3.2.1. Water Column Samples

Three vertical casts were performed over the ZGP, collecting water samples at 50 m, 100 m water depth, and at the sea bottom using Niskin bottles (Figure 3a). Two vertical casts were performed away from the fluid emissions area to obtain background values (Figures 3b and 3c). The samples for dissolved gas analysis were collected with the Niskin bottles and stored in 240 mL Pyrex bottles. Water was transferred from the Niskin to the Pyrex bottle using a silicon tube with the tube end placed at the bottom of the Pyrex bottle to minimize turbulence. After filling, the Pyrex bottles were sealed using rubber/teflon septa and custom-built pliers. The samples were stored keeping the sealed necks submerged in sea water until they were transferred to the laboratory. Laboratory analyses of the samples were conducted within 2 weeks. Details about the sampling and dissolved gas extraction methods are described in *Italiano et al.* [2009a, 2014a].

##### 3.2.2. Gas Bubble Samples

Four ROV dives (Figure 3a) were conducted to collect water and gas samples. Samples of the bubbling gases were taken by using an ROV equipped with a manipulator. A water-filled, inverted, 50 mL glass bottle was positioned over the bubble column streams and filled halfway with gas prior to bringing the ROV (and the

upside down bottle) back to the surface. During the ascent the gas expanded and pushed out most of the remaining water. At the surface an operator fixed a gas-tight cap on the bottle, which was stored submerged in sea water to avoid any atmospheric contamination before undergoing laboratory analyses.

### 3.2.3. pCO<sub>2</sub> Probe Transects

A GasPro pCO<sub>2</sub> probe was mounted on the ROV for in situ monitoring during the various dives. These probes, developed at Sapienza University of Rome [Graziani *et al.*, 2014], use a thin Teflon AF membrane to equilibrate CO<sub>2</sub> dissolved in the surrounding water with a small air-filled chamber holding a miniature nondispersive infrared detector. The units have a T<sub>90</sub> response time of about 7 min (i.e., the time required for the sensor to reach 90% of the actual value); this time is controlled by gas diffusion rates across the membrane, membrane diameter, sensor volume, and water flow dynamics. Each probe is also equipped with a water temperature sensor, which has a T<sub>90</sub> of about 45 s. During deployment the probes were always on, registering values once every 60 s.

### 3.3. Geochemical Analyses

Chemical and isotopic analyses were performed in the laboratory on both dissolved and bubbling gas samples. Chemical analyses were performed by gas chromatography (GC) (Perkin Elmer Clarus500 equipped with a double TCD-FID detector) using argon as the carrier gas. Typical uncertainties are within ± 5%. The samples of bubbling gases were transferred from the Pyrex bottles by puncturing its septum with a syringe, drawing the gas, and injecting it into the GC. The dissolved gases were extracted from the 240 mL water samples after equilibration at constant temperature with a host-gas (high-purity argon) injected in the sample bottle through the rubber septum (for further details, see *Italiano et al.* [2009a, 2014a]).

The He-isotope ratio in free-gas samples was analyzed directly from the sample bottles after purification in the high-vacuum inlet line of the mass spectrometer. The isotopic composition of dissolved He was analyzed by headspace equilibration, following the method proposed by *Italiano et al.* [2014a]. He and Ne were then cryogenically separated and admitted into mass spectrometers. The <sup>3</sup>He/<sup>4</sup>He ratio and <sup>20</sup>Ne content were analyzed by a GVI Helix SFT mass spectrometer. Helium isotope compositions are given as R/R<sub>A</sub>, namely <sup>3</sup>He/<sup>4</sup>He of the sample versus the atmospheric <sup>3</sup>He/<sup>4</sup>He ratio (R<sub>A</sub> = 1.386 × 10<sup>-6</sup>). Measured values were corrected for atmospheric contamination of the sample (R<sub>C</sub>/R<sub>A</sub>) on the basis of the <sup>4</sup>He/<sup>20</sup>Ne ratio [Sano and Wakita, 1988]. The <sup>4</sup>He/<sup>20</sup>Ne ratio was measured by peak intensities on the mass spectrometer. Typical uncertainties in the range of low <sup>3</sup>He samples are within ± 5%.

The stable isotopic composition of CO<sub>2</sub>-C of the bubbling gases was analyzed by a mass spectrometer (Finnigan MAT Delta S) after purifying the CO<sub>2</sub> under vacuum. δ<sup>13</sup>C values of the total dissolved carbon (δ<sup>13</sup>C<sub>TDC</sub>) was measured on 2 mL of water sample introduced in bottles where high-purity helium was injected to remove atmospheric CO<sub>2</sub>. The water samples were acidified with phosphorus pentoxide in an autosampler to ensure complete release of CO<sub>2</sub> from acidified waters. CO<sub>2</sub> was then directly admitted to a continuous flow mass spectrometer (AP2003). The results are reported in δ<sup>13</sup>‰C values relative to the VPDB (Vienna Peedee Belemnite) standard; standard deviation of the <sup>13</sup>C/<sup>12</sup>C ratio was ± 0.2‰.

## 4. Results

### 4.1. Gas Composition

Table 3 lists the analytical results for the bubbling gases, including chemical composition expressed in volume % and isotopic ratios of helium, carbon, and <sup>4</sup>He/<sup>20</sup>Ne. The chemical composition of the dissolved gas phase (Table 3), expressed in cm<sup>3</sup> at Standard Temperature and Pressure per liter of water (cm<sup>3</sup>STP/L<sub>H<sub>2</sub>O</sub>), was calculated starting from the gas-chromatographic analyses and combining the solubility coefficients (Bunsen coefficient "β", cm<sup>3</sup><sub>gas</sub>/mL<sub>water</sub> STP) of each gas species, the volume of gas extracted (cm<sup>3</sup>), the water sample volume, and the equilibration temperature, as shown in equation (1):

$$G_C = \{ [G_{gc}] * V_{\gamma_e} + ([G_{gc}] * \beta_G * VW) \} VW^{-1} * V_{\gamma_e} * V_{\gamma_i}^{-1} / 100 \quad (1)$$

where G<sub>C</sub> is the concentration of the selected gas species, G<sub>gc</sub> is its concentration measured by gas chromatography (volume %), and V<sub>γ<sub>e</sub></sub> and V<sub>γ<sub>i</sub></sub> represent the extracted and the introduced gas volumes, respectively, while VW is the volume of the analyzed water sample (see also *Italiano et al.* [2009a, 2014a] for further details). All volumes were carefully measured at the equilibration temperature.

**Table 3.** Chemical and Isotopic Composition of the Dissolved and Bubbling Gases<sup>a</sup>

#	Sample Depth	He	H <sub>2</sub>	O <sub>2</sub>	N <sub>2</sub>	CO	CH <sub>4</sub>	CO <sub>2</sub>	He/Ne	R/Ra	R/Ra <sub>c</sub>	Error	δ <sup>13</sup> C <sub>TDC</sub>	δ <sup>13</sup> C <sub>CH4</sub>
<i>Dissolved Gases</i>														
1	BT3-2 50 m		1.3 × 10 <sup>-2</sup>	4.93	11.03	2.5E - 05	7.1 × 10 <sup>-4</sup>	0.56	0.29	0.80	---	---	-0.67	n.a.
2	BT3-2 100 m		1.6 × 10 <sup>-2</sup>	4.21	9.84	1.4E - 05	9.4 × 10 <sup>-4</sup>	0.58	0.34	0.86	---	---	-0.57	n.a.
3	BT3-1 bottom	2.3 × 10 <sup>-4</sup>	7.0 × 10 <sup>-3</sup>	4.64	10.96	1.3E - 05	1.8 × 10 <sup>-3</sup>	0.72	0.32	1.02	---	---	n.a.	n.a.
4	BT4-3 50 m		2.4 × 10 <sup>-3</sup>	4.02	8.10	1.3E - 05	9.2 × 10 <sup>-4</sup>	0.59	0.33	0.89	---	---	-0.25	n.a.
5	BT4-2 100 m		4.7 × 10 <sup>-3</sup>	3.96	9.76	2.0E - 05	1.4 × 10 <sup>-3</sup>	0.58	0.32	0.88	---	---	-1.59	n.a.
6	BT4-2 bottom		1.2 × 10 <sup>-3</sup>	3.66	7.99	2.0E - 05	7.5 × 10 <sup>-4</sup>	0.70	0.34	0.94	---	---	-0.13	n.a.
7	BT6-3 50 m		1.6 × 10 <sup>-3</sup>	4.44	10.76	3.0E - 05	3.3 × 10 <sup>-4</sup>	0.46	0.33	0.85	---	---	-0.95	n.a.
8	BT6-2 100 m		7.0 × 10 <sup>-3</sup>	4.41	10.84	1.8E - 05	2.7 × 10 <sup>-4</sup>	0.56	0.24	0.83	---	---	-0.91	n.a.
9	BT6-1 bottom		1.5 × 10 <sup>-2</sup>	2.37	7.77	1.4E - 05	8.1 × 10 <sup>-4</sup>	0.72	0.35	0.89	---	---	n.a.	n.a.
10	BT8-1 bottom		4.3 × 10 <sup>-3</sup>	4.22	10.23	2.3E - 05	1.1 × 10 <sup>-4</sup>	0.53	0.32	0.85	---	---	n.a.	n.a.
ASSW		4.8 × 10 <sup>-5</sup>		4.80	9.60		1.0 × 10 <sup>-6</sup>	0.24						
<i>Bubbling Gases</i>														
#	Sample Depth	He	H <sub>2</sub>	O <sub>2</sub>	N <sub>2</sub>	CO	CH <sub>4</sub>	CO <sub>2</sub>	He/Ne	R/Ra	R/Ra <sub>c</sub>	Error	δ <sup>13</sup> C <sub>CO2</sub>	δ <sup>13</sup> C <sub>CH4</sub>
11	BT1-129 m	7.9 × 10 <sup>-3</sup>	7.0 × 10 <sup>-4</sup>	12.25	33.40	1.9 × 10 <sup>-4</sup>	2.6 × 10 <sup>-4</sup>	50.94	7.71	3.49	3.60	0.02420	n.a.	-43.70
12	BT1-129 m	8.2 × 10 <sup>-3</sup>	9.0 × 10 <sup>-4</sup>	11.34	31.87	1.3 × 10 <sup>-4</sup>	2.6 × 10 <sup>-4</sup>	55.08	7.11	3.50	3.62	0.02434	n.a.	n.a.
13	BT4-127 m	5.8 × 10 <sup>-3</sup>	bdl	12.75	30.28	1.9 × 10 <sup>-4</sup>	1.9 × 10 <sup>-4</sup>	54.22	5.47	3.41	3.56	0.02395	n.a.	n.a.
14	BT4-127 m	6.4 × 10 <sup>-3</sup>	bdl	13.62	35.98	bdl	2.1 × 10 <sup>-4</sup>	48.93	10.19	3.48	3.56	0.02394	n.a.	-43.63

<sup>a</sup>Dissolved gases were extracted from the water samples collected by the vertical casts, bubbling gases collected at the emission point close to the seafloor. The chemical composition of the dissolved gases is given in ccSTP/liter of sea water. Bubbling gas composition in vol %. n.a. = not analyzed. bdl = below detection limits. The numbers in italics indicate ASSW gas composition.

The CO<sub>2</sub> content, with concentrations in the range of 48.9–55.1% for the bubbling gases and ranging from 0.46 to 0.72 cm<sup>3</sup>/L<sub>H<sub>2</sub>O</sub> for the dissolved gas phase (Table 3), is by far the most abundant component of the gas phase. Oxygen and nitrogen range from 2.3 to 4.9 and 7.7 to 11 cm<sup>3</sup> STP/L, respectively, for the dissolved gases and between 11.3–13.6% and 30.2–35.9%, respectively, for the bubbling gases. Amongst the other components CH<sub>4</sub> is always detected in concentrations ranging from 1.1 × 10<sup>-4</sup> to 1.8 × 10<sup>-3</sup> cm<sup>3</sup>/L<sub>H<sub>2</sub>O</sub> and in concentrations between 1.7 and 2.6% for the bubbling gases. The average dissolved gas composition in Air-Saturated Sea Water (ASSW) is reported for comparison in Table 3 and shows that the dissolved CH<sub>4</sub> is 2 orders of magnitude above saturation with the atmosphere (ASSW value equal to 10<sup>-6</sup> cm<sup>3</sup>/L<sub>H<sub>2</sub>O</sub>).

Ternary plots (Figures 4a and 4b) show the contemporary presence in the extracted gases of atmospheric components (O<sub>2</sub> + N<sub>2</sub>, Figure 4a) as well as of geogenic CO<sub>2</sub> and CH<sub>4</sub>. The plot along the ASSW-CO<sub>2</sub> mixing line highlights the injection of CO<sub>2</sub>-dominated volatiles into an ASSW. Figure 4b highlights the occurrence of gas-water interactions inducing CO<sub>2</sub> dissolution and enhancing the less soluble species concentrations (e.g., CH<sub>4</sub>) in the dissolved gas assemblage.

The δ<sup>13</sup>C<sub>TDC</sub> values measured in the dissolved gases (from -1.59‰ to -0.13‰) fall in the range of various deep, inorganic sources, such as metamorphic decarbonation of marine carbonates or degassing of mantle-derived products. Although the variable isotope fractionation due to dissolution processes in sea water likely occurs, the recorded values rule out any major contribution from organic sources. The carbon isotopic composition of CH<sub>4</sub> in bubbling gases, close to -43‰ (Table 3), points to a thermogenic origin and is consistent with an enrichment of CH<sub>4</sub> in the hydrothermal fluids (see Figure 4b) due to geothermal reequilibration, as already observed in submarine systems [Italiano and Nuccio, 1991]. This suggests the existence of a geothermal reservoir where the ascending volatiles equilibrate.

The <sup>4</sup>He/<sup>20</sup>Ne ratio (Table 3) can be used as an indication of atmospheric contamination of deep volatiles. The <sup>4</sup>He/<sup>20</sup>Ne ratio of any dissolved gas sample is expected to be very close to atmospheric values; however, our dissolved gas samples (Table 3) show slight but detectable deviations relative to 0.267 (assumed to be the representative <sup>4</sup>He/<sup>20</sup>Ne value for ASSW [Holoher et al., 2002]). Considering that all neon is of atmospheric origin, any increase of the <sup>4</sup>He/<sup>20</sup>Ne ratio indicates helium addition from a Ne-poor source, namely from a crustal or magmatic source. The helium isotopic ratios in all the gas extracted from water samples collected both in proximity of the vents (BT 3, 4) and away from them (BT 6, 8) are indistinguishable from the atmospheric value. In contrast, helium isotopes and <sup>4</sup>He/<sup>20</sup>Ne ratios of the bubbling gases display very low atmospheric contamination. In particular, measured values of <sup>4</sup>He/<sup>20</sup>Ne range between 5.4 and 10.2 and are 15–30 times those of atmospheric air. The measured <sup>3</sup>He/<sup>4</sup>He values of up to 3.6 Ra (Ra = atmospheric <sup>3</sup>He/<sup>4</sup>He

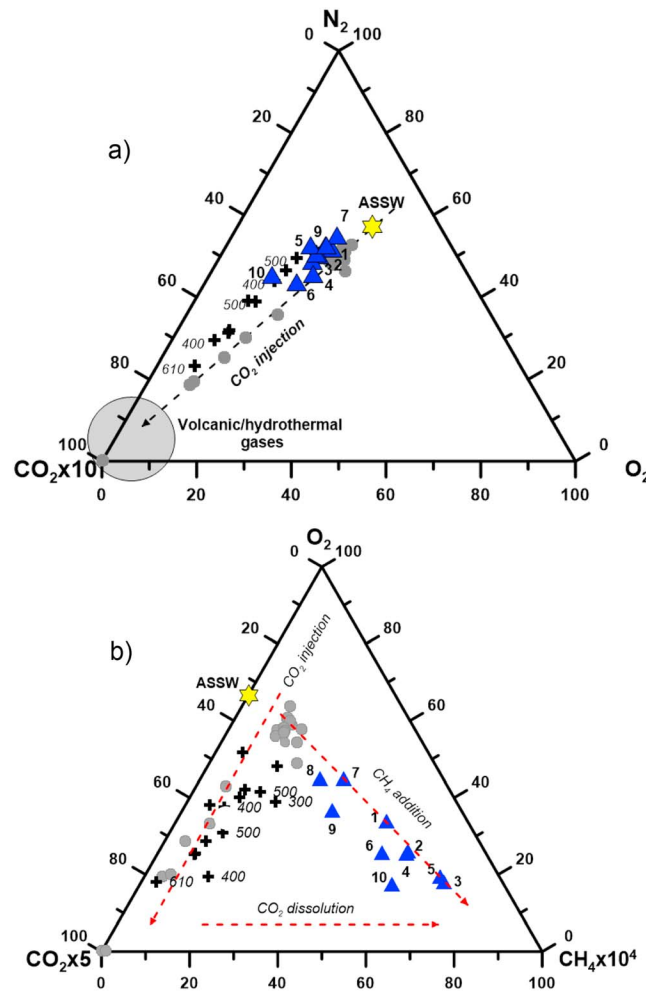


**Figure 4.** Geochemical features of the dissolved gases. (a) O<sub>2</sub>-N<sub>2</sub>-CO<sub>2</sub> ternary diagram for gas samples. The samples plot between the Air-Saturated Sea Water mark (ASSW, yellow star) and the CO<sub>2</sub> vertex. The dashed black line indicates a trend of CO<sub>2</sub> injection in an ASSW. Blue triangles = dissolved gases from Pontine Island with sample ID labeled as in Table 2; black crosses = samples from Marsili seamount [after Italiano et al., 2014b]; grey-filled circles = samples from Capo Vaticano seamount [after Loreto et al., 2015]. The numbers in italics = Marsili samples depths. (b) CH<sub>4</sub>-O<sub>2</sub>-CO<sub>2</sub> ternary diagram for gas samples showing the relative concentrations of volcanic/hydrothermal-derived components (CO<sub>2</sub>-CH<sub>4</sub>) together with the dissolved atmospheric component (here represented by oxygen). The dashed red arrows = trends of CO<sub>2</sub> injection (modifying the dissolved gas assemblage) and CO<sub>2</sub> dissolution due to gas/water interaction enhancing the less soluble gas species like CH<sub>4</sub>. Symbols are the same as in Figure 4a.

A clear 0.65°C peak is observed in the ROV-3 data, while small, variable peaks up to 0.2°C occur in ROV-6 bis. The generally stable temperature values imply a lack of thermal waters being released in the gas leakage areas; however, the small anomalies indicate the potential for low-flux, spatially restricted thermal water release; more detailed study would be needed to address this issue.

All dives begin and end with pCO<sub>2</sub> values of 350–400 μatm (Figures 6a–6e), which is equivalent to the concentration in air or the pCO<sub>2</sub> value of surface water in contact with the atmosphere. At the beginning of all dives pCO<sub>2</sub> values decrease by 50–100 μatm and then recover over the first 10–15 min, as the probe equilibrates with the continually increasing surrounding pressure. Once at depth, values restabilize or increase. The five dives are in leakage areas in water depths from 118 to 128 m. Of these, only ROV-4 (Figure 6b) does

ratio =  $1.39 \times 10^{-6}$ ) are significantly higher than those measured in terrestrial CO<sub>2</sub>-dominated gas emissions from the Larderello geothermal field (0.5–3.2 Ra [Minissale, 2004]); the Roman Comagmatic province (lower than 2 Ra [Martelli et al., 2004; Italiano et al., 2008]); Mount Vesuvius (2.2–2.7 Ra [Italiano et al., 2000]); and Solfatara within the Phlegraean fields (2–3.2 Ra [Italiano et al., 2000]). They are, instead, close to those normally recorded at Stromboli and Panarea volcanoes (4–4.2 Ra from both the edifices). Our samples clearly fall in the same range as submarine vents in the Aeolian Islands (Figure 5). These are among the lowest values measured in active volcanoes from subduction zones worldwide [Italiano, 2009b]. Those ratios are interpreted as resulting from magmatic products that were generated by a parental mantle contaminated by the subduction of crustal rocks [Martelli et al., 2004].

#### 4.2. In Situ CO<sub>2</sub> and Temperature Measurements

The temperature values measured by the GasPro sensors (Figure 6) clearly indicate the ROV descent and seafloor surveying periods, since temperature values rapidly decrease from around 20–22°C at the sea surface to about 15°C at the seabed. For most dives the water temperature values are fairly stable near the seabed, although some small peaks are observed in correspondence with observed bubbling (blue shaded area). A

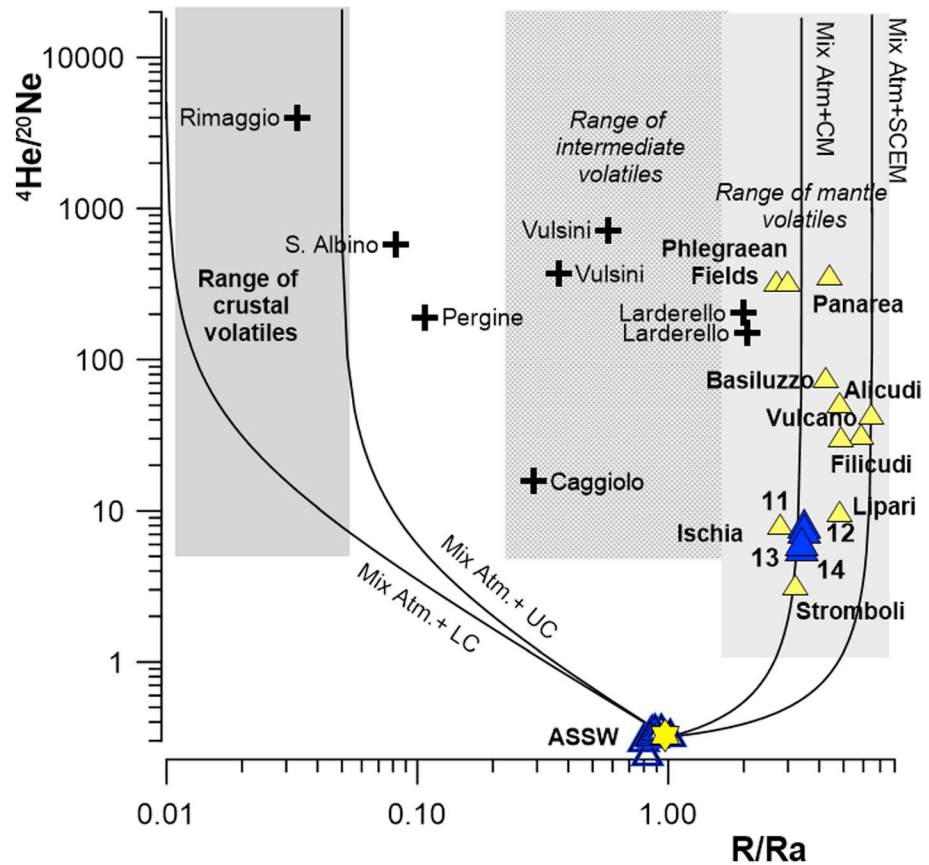


**Figure 5.** Plot of  $^4\text{He}/^{20}\text{Ne}$  versus uncorrected  $R/R_a$  values. The open and filled blue triangles show the dissolved and bubbling gases, respectively. Yellow triangles = bubbling gases from the Aeolian Islands, Ischia and Plegraean Fields. Black crosses = bubbling gases from the central Apennines. The black lines = mixing of atmospheric helium (atm) with helium from crustal and mantle sources. Assumed end-members are contaminated mantle (CM, 3.4  $R_a$  and  $\text{He}/\text{Ne}$  ratio = 1000); Subcontinental European Mantle (SCEM, 6.5  $R_a$  and  $\text{He}/\text{Ne}$  ratio = 1000); lower crust (LC, 0.01  $R_a$  and  $\text{He}/\text{Ne}$  = 5000), and upper crust (UC, 0.05  $R_a$  and  $\text{He}/\text{Ne}$  = 5000). Error bars are smaller than the plotted symbols. IDs for Pontine bubbling gases are the same as in Table 2. Data after Italiano *et al.* [2008], Italiano *et al.* [2009a, 2014b], and Dunai and Baur [1995]. The grey areas broadly represent the typical ranges for mantle, intermediate, and crustal volatiles. Pontine gas samples fall in a range typical of mantle volatiles.

not show a clear  $p\text{CO}_2$  anomaly. The other dives show maximum  $p\text{CO}_2$  values of 550  $\mu\text{atm}$  for ROV-3, 1100  $\mu\text{atm}$  for ROV-6 bis, 785  $\mu\text{atm}$  for ROV-7, and 1630  $\mu\text{atm}$  for ROV-8. Values typically start to rise sharply

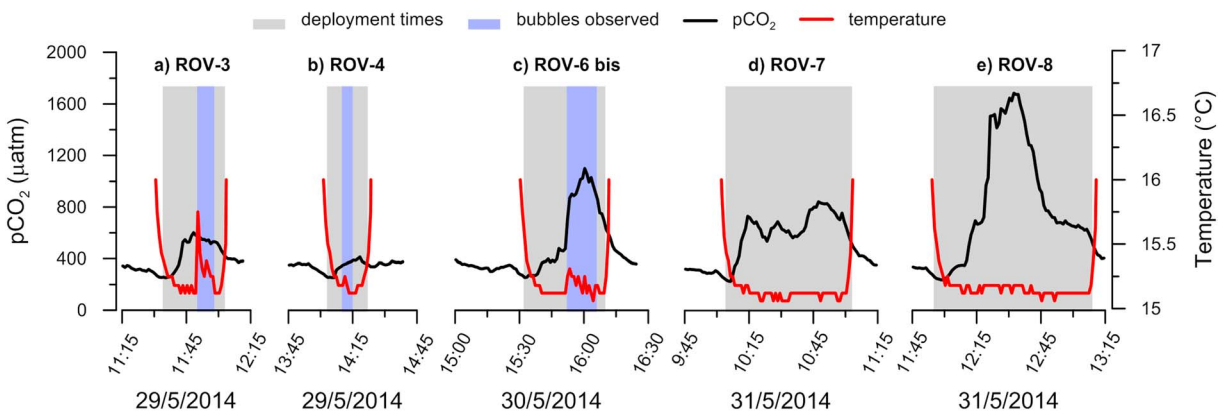


**Figure 6.** (a–e) GasPro temperature and  $p\text{CO}_2$  data from five ROV dives. Grey boxes indicate the time windows when the ROV was at the near seafloor, while blue boxes indicate periods during which gas bubbles were visually observed.

once the ROV has reached the seafloor within the ZGP, although it is interesting to note that the sharpest  $p\text{CO}_2$  rise in ROV-6 bis corresponds with small temperature anomalies and the observation of bubbles. In ROV-3 and ROV-7 the  $p\text{CO}_2$  values remain elevated until the ROV starts its ascent, whereas in ROV-6 bis and, especially, ROV-8 the values peak in the middle of the deployment and start to decrease even while the probe is still near the seafloor. Results from the latter two deployments imply spatial and temporal variability within the ZGP, caused by localized leakage points and marine currents.

Note that because the GasPro  $p\text{CO}_2$  sensor has an approximate 7 min equilibration time, the results represent temporally averaged values that may underestimate some short-term higher concentrations. Instead, the temperature values are expected to be relatively close to the true values given that sensor's short  $T_{90}$  (45 s) relative to the 60 s sampling interval.

### 4.3. Morphological Evidence of Widespread Fluid-Venting Activity

The analysis of the high-resolution multibeam bathymetry highlights the occurrence of several areas characterized by seabed structures generated by fluid emissions.

Apart from the ZGP (described in section 2.2), four other large depressions (length  $>250$  m) can be distinguished (depressions DA-DD in Figures 2 and 7) on the Zannone insular shelf. They are located both in the northwestern and eastern sectors, in water depths ranging between 126 and 146 m (Figure 2). Clear evidence of fluids vented from the seafloor has been found within depression DA. They are represented by a fluid plume observed on ROV videos (Figure 7f).

Depression DA (Figure 7b) is located 8 km from the northeastern sector of Zannone Island, in water depth varying from 135 to 148 m. The depression is 550 m long, 300 m wide, and elongated in the NW-SE direction. It covers an area of  $0.16 \text{ km}^2$  and is about 13 m deep. DA has a subelliptical shape, with asymmetric and steep (slope gradients up to  $15^\circ$ ) bounding scarps that are more defined along its northern sector where they have a step-like morphology. The floor of depression DA is located at about 148 m depth and characterized by a rather flat morphology (bathymetric cross section shown in Figure 7e). It is characterized by small morphological highs and ridges that are about 1–2 m high. Elongated pockmarks are also present in the NW sector along the bounding escarpment (Figure 8a). The seafloor outside the DA is characterized by the occurrence of some pockmarks; one of these is characterized by a complex morphology that is probably due to the coalescence of different pockmarks (Figure 8a).

Depression DB (Figure 7c) is located 3.5 km off the northwestern sector of Zannone Island, in water depths varying from 130 to 142 m. It is 1000 m long, 350 m wide (surface area of  $0.3 \text{ km}^2$ ), and 12 m deep and is characterized by an elongate and irregular shape with a NE-SW trend. It is bounded by arcuate scarps with a gentle slope (average slope of  $5^\circ$ ) that appear more defined along its southeastern and eastern sectors. In the NE and central sectors, elongated pockmarks are present along the bounding escarpment (Figure 8c). Within the depression, the seafloor morphology is uneven (Figure 8b and bathymetric cross section of Figure 7e) and characterized by isolated cone-shaped features (about 30 m wide and 1 m high) and pockmarks (about 80 m long, 20 m wide, and 0.5–5 m deep) that in some cases are elongated. A main pockmark occurs in the eastern sector of DB. It is a 180 m wide and 5 m deep subcircular depression, characterized by a complex morphology including a flat seafloor bounded by elongated pockmarks. Isolated cone-shaped features are mainly concentrated in the western and central sectors of the DB (Figure 8b), although some are also present on the seafloor surrounding the eastern sector of the DB.

Depression DC (Figure 7d) is located about 3 km from the northwestern sector of Zannone Island, in water depths varying from 127 to 140 m. It is 500 m long, 400 m wide (surface area of  $0.12 \text{ km}^2$ ), and 2–7 m deep and is characterized by a subcircular shape with well-defined circular and subcircular bounding scarps having average slope of  $10^\circ$ . In a limited area of the SW sector, bounding scarps have a step-like morphology. The floor of depression DC is quite regular (Figures 7d and 7e). However, in the central sector of the DC, the seafloor is characterized by a 350 m wide mound with an irregular morphology. The floor of the depression is also characterized by elongated pockmarks (about 50 m long and 10 m wide) located close to the bounding scarps (Figure 8c). A small N-S elongated ridge (about 40 m long and 1.5 m high) occurs in the northern sector of the DC.

Depression DD (Figure 7d) is located about 2.7 km from the northern sector of Zannone Island, close to depression DC, in water depths ranging between 126 and 133 m. It is 720 m long, 300 m wide (surface area

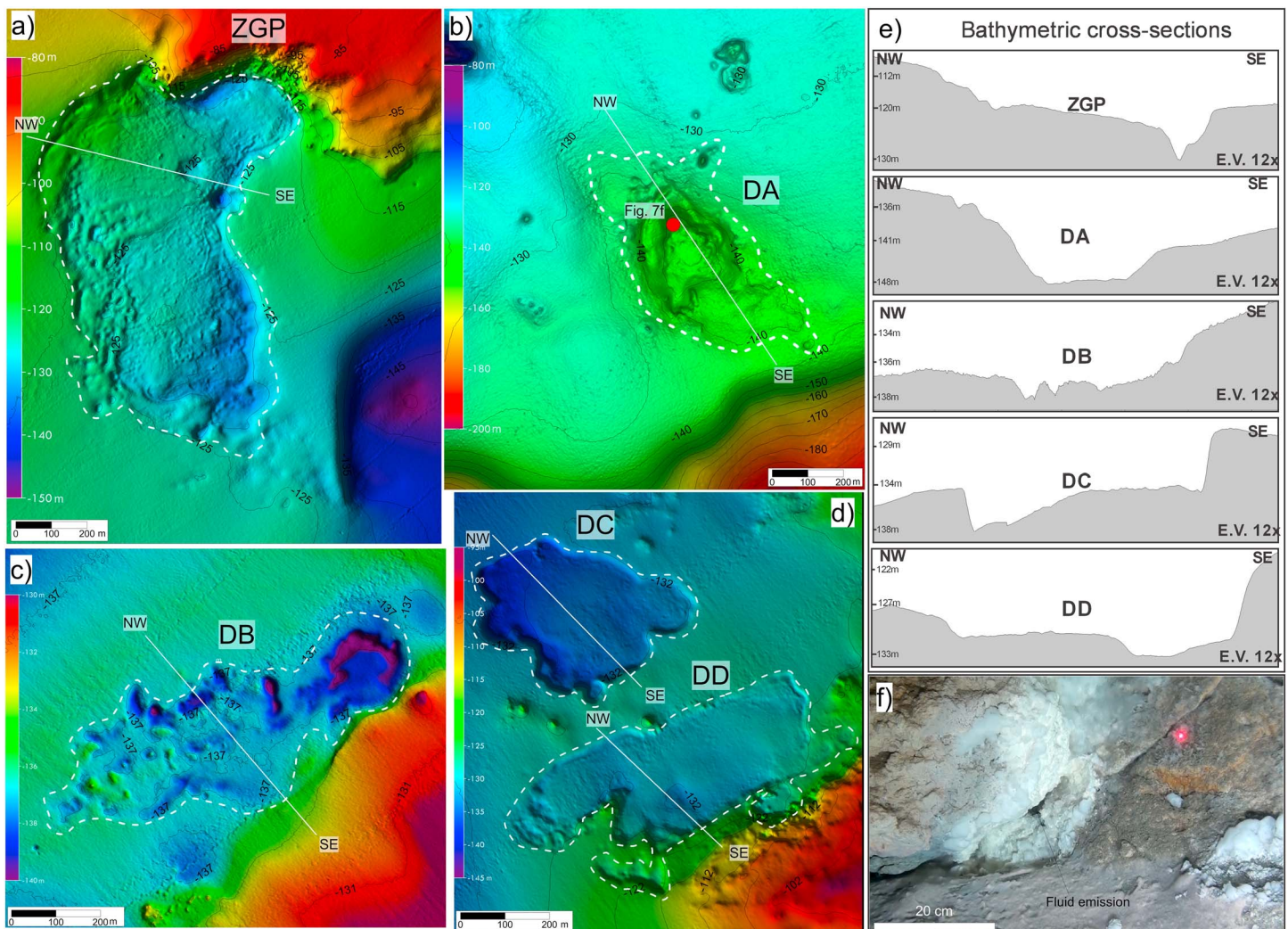


**Figure 7.** Shaded relief of multibeam bathymetry showing the morphology of the giant depressions individuated offshore Zannone Island: (a) depression ZGP, (b) depression DA, (c) depression DB, (d) depressions DC and DD, and (e) bathymetric cross sections relative to the giant depressions. (f) ROV image showing active fluid emission within depression DA.

of 0.14 km<sup>2</sup>), and 2–10 m deep. It has an elongate shape oriented NE-SW and is bounded by straight and steep (10–28°) NE-SW scarps that are more defined along the southern sector. The southern boundary of the DD corresponds to the outcrop of a rocky substrate, forming a well-defined, 20 m high escarpment and in a limited area of the SW sector: bounding scarps approach a step-like morphology. Along the northern boundary the negative relief is of 2–3 m. Almost all the floor of depression DD has a regular and flat morphology (Figures 7d and 7e). However, small elongated pockmarks (about 180 m long and 10 m wide) are located close to the northern and eastern bounding escarpments. Moreover, subcircular pockmarks (about 70 m long and 40 m wide) are found near its western and southern boundaries (Figure 8d).

The seafloor outside the DD is characterized by isolated cone-shaped features and small pockmarks (Figure 7 d).

## 5. Discussion

### 5.1. Existence of an Undocumented Geothermal System Off Zannone Island

The multibeam bathymetry shows that the four depressions (DA, DB, DC, and DD) are morphologically similar to the ZGP described by *Ingrassia et al.* [2015], even if they are smaller in size and their seabed morphology is less complicated. More in detail, depressions DB, DC, and DD are similar for the occurrence of mounds, small

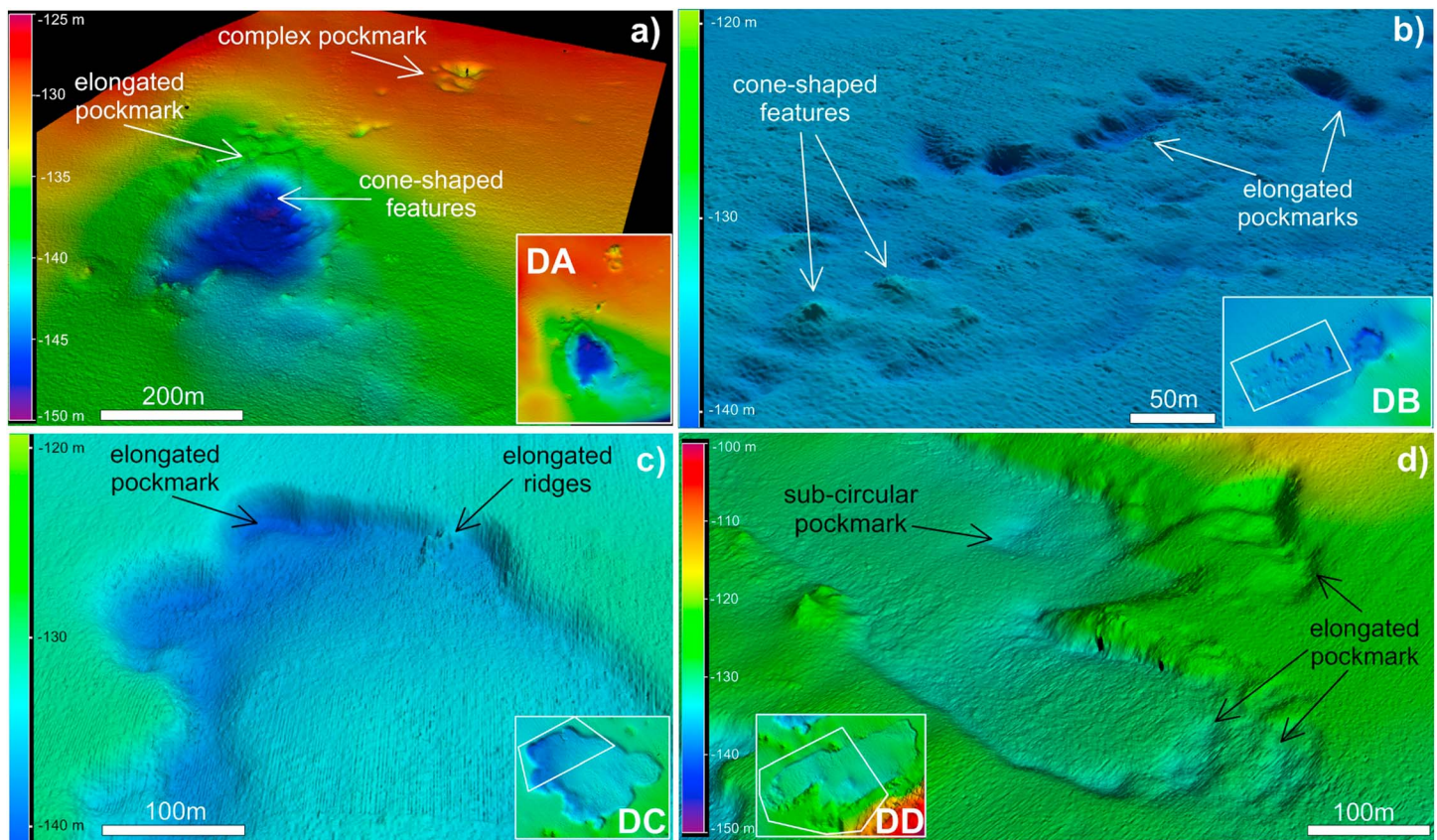


**Figure 8.** Shaded relief of multibeam bathymetry showing the detailed morphology of the large depressions: (a) depression DA, (b) depression DB, (c) depression DC, and (d) depression DD.

cones, ridges, and pockmarks. In addition, elongated pockmarks frequently occur either at the base of the bounding scarps (depressions DB, DC, and DD) or near their upslope break (e.g., depressions DA and DD). Elongated pockmarks are usually attributed to the action of strong bottom currents [Judd and Hovland, 2007]. In the study area, however, they seem to be mostly due to the coalescence of smaller features. In some cases (e.g., depressions DC and DD) the bounding scarps are characterized by subcircular to subrectilinear trends and a step-like morphology that resemble those observed at the ZGP.

In general, the large size and complex shape of these depressions appears to be the result of the coalescence of different pockmark/crater-like features, 50 to 350 m wide (e.g., depressions DA, DB, and DC). A similar situation has been observed at the ZGP, where the complex shape seems to be related to the coalescence of 200 to 500 m wide crater-like features [Ingrassia *et al.*, 2015].

Because of these morphological characteristics, we interpret the four depressions as complex fluid-escape features. This interpretation is further supported by the direct observation of fluid venting within depression DA (Figure 7f) and of bacterial mats, small pockmarks, and authigenic mounds within depression DC [Ingrassia, 2016]. Based on these characteristics it is possible to argue that fluid emission activity in these depressions has been developing with the same modality as in the ZGP, including (1) vigorous-explosive events that produce pockmarks and crater-like morphologies and (2) steady or semisteady seepage that generate lithified sediments, crusts, and domal structures and sustain bacterial mats activity.

The composition of the venting fluids (relevantly enriched in  $\text{CO}_2$ ) and the presence of these seabed depressions imply that the seafloor surrounding Zannone Island is affected by widespread and ongoing hydrothermal emissions. Based on the isotopic signature (Figure 5) we speculate that this phenomenon represents the surface manifestation of a deep and unknown geothermal system. This interpretation would also explain the warm sediment with a strong sulphur smell, collected in the northern sector of the ZGP, the temperature

anomalies measured by the ROV-mounted probe, and the sulphur springs located at Grottelle and Cavone del Lauro on Zannone Island (reported by *Tricoli* [1855]).

Widespread hydrothermal activity occurs on the shallow flanks and in the breached calderas of numerous arc volcanoes in the Mediterranean Sea [*Hannington et al.*, 2005, and reference therein]. The discovery of the Zannone hydrothermal field updates the record of seafloor hydrothermal systems of the Tyrrhenian Sea, supporting the evidence that extensional back-arc basins and their margins represent likely settings for hydrothermal venting. In particular, the fluid emissions observed off Zannone Island have geochemical characteristics (i.e., CO<sub>2</sub>-enriched fluids derived by a contaminated mantle) that are similar to those described in shallow water area of the Tyrrhenian Sea (e.g., offshore Panarea and Vulcano Islands). The seabed structures are also similar, even if they differ for the larger dimension, more complex morphology, and structure of the depressions. This implies a long-lasting activity (at least hundreds of years) that included paroxysmal events able to produce crater-like depressions with dimensions of up to 0.5 km<sup>2</sup>.

As frequently observed, faults may provide a significant control on formation of fluid-escape features [e.g., *Pilcher and Argent*, 2007]. In addition, the distribution of seafloor fluid seeps can be associated with subsurface structures, such as polygonal faults, salt diapirs, paleocanyons, etc. [e.g., *Gay et al.*, 2007]. The Zannone hydrothermal field is located on the Ponza-Zannone structural high, a 40 km long, NE-SW trending tectonic structure that is situated on the eastern sector of the Tyrrhenian continental margin (Figure 1b). Here, during the Plio-Pleistocene, extensional processes produced widespread volcanic activity [e.g., *De Rita et al.*, 1986; *Conte and Dolfi*, 2002]. Volcanic units are emplaced above a basement mostly composed of Meso-Cenozoic sedimentary rocks (mainly dolomitic limestones) and dissected by fault networks (Figure 1b). The prevolcanic substratum topographically culminates at Zannone Island, where it crops out.

This stratigraphic and tectonic setting would explain the occurrence of the hydrothermal depressions offshore Zannone Island. In fact, bathymetric data show that these depressions occur only on the west and east side of Zannone Island, on the outer shelf (Figures 1b and 2), suggesting that the NE-SW trending faults bounding the Ponza-Zannone structural high and the shallow fractured basement are favorable conditions for the upward migration of deep hydrothermal fluids and their seepage through the seafloor (Figure 9). These factors, along with the presence of a heat source, contributed to the development of the hydrothermal systems and the clearly defined seafloor structures.

More in detail, all the depressions (DA to DD and ZGP) developed in a similar geological environment consisting of a thin sedimentary cover (<75 m [*Zitellini et al.*, 1984]), including sandy sediment in the shallow subsurface, that rests on a faulted rocky basement [*Ingrassia*, 2016]. According to the model shown in Figure 9, the regional faults affecting the Zannone high provide possible pathways for fluid migration. However, a precise definition of the shallow subsurface structures and a direct correlation between faults and location/shape of the depressions are difficult, because existing seismic data [*Zitellini et al.*, 1984] offer a regional overview of the subsurface. Based on morpho-bathymetric data, a possible indication of a tectonic or structural control may be provided by the subrectilinear trend of some bounding escarpments (sectors of depressions DD and DC) and elongated shape of depressions DD and DB, which are subparallel to the NE-SW regional faults (Figure 1b); however, others have a subcircular shape (DC) or are elongated transversely to the NE-SW regional faults (DA and ZGP). In addition, there is no evidence of major faulting on the seabed (e.g., well-defined fault scarps), both within the depressions and in adjacent areas.

All this would suggest that even if the upward migration of hydrothermal fluids seems to be controlled by major faults, the association between seafloor depressions and major faults is unlikely. It is possible, however, that there is an association with minor faults or fractures, which are not resolved by available seismic data, and/or with stratigraphic heterogeneities of the shallow subsurface; moreover, hydrothermal circulation and associated processes would impose additional heterogeneity [e.g., *Fisher*, 2004], affecting flow patterns and distribution of seafloor fluid seeps. Although further studies are needed to address this issue, we point out that complex mechanisms should control fluid flow patterns and formation of the studied depressions. In fact, their present-day morphology would testify occurrence of multiple episodes of vigorous/explosive fluid emission, possibly favored by mechanisms of self-sealing due to the formation of authigenic pavements and collapse of sediment, as proposed by *Ingrassia et al.* [2015] for the ZGP.

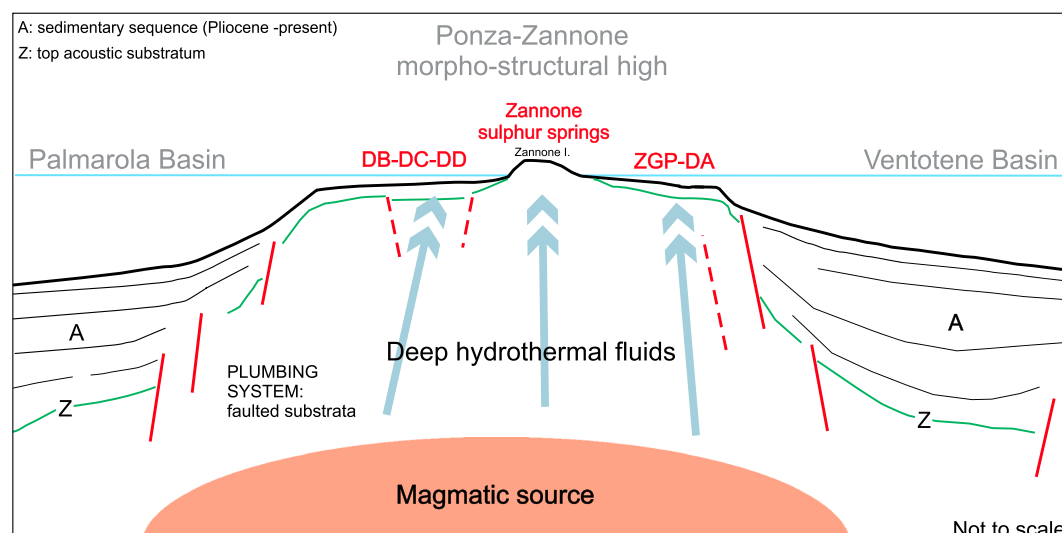


**Figure 9.** Sketch of the structural setting of the Ponza-Zannone morpho-structural high with indication of the Zannone hydrothermal field and main faults (see text for discussion).

This complex interplay between controlling factors, along with the occurrence of repeated paroxysmal events of fluid emission, might explain the morphological complexity of the giant depressions and make the Zannone hydrothermal field rather peculiar when compared with other known submarine hydrothermal fields observed in shallow water (e.g., the Panarea craters [Monecke *et al.*, 2012]).

### 5.2. Possible Nature of the Deep Geothermal System

The geochemical signature of the collected fluids provides information of active CO<sub>2</sub>-dominated degassing with a significant contribution of mantle volatiles. This result is peculiar for the study area where active volcanism is unexpected, since the last volcanic cycle dates back to the Pleistocene [e.g., Cadoux *et al.*, 2005]. The vented volatiles may originate in the mantle, driven to the surface along lithospheric faults. The crustal thickness of about 25 km makes a direct mantle degassing unlikely because of permeability considerations [Italiano *et al.*, 2000, and references therein]. Moreover, under this perspective the vented volatiles should also show an enhanced crustal contribution (<sup>4</sup>He enrichment), in contrast with our <sup>3</sup>He-rich data. Although a role of lithospheric faults is not excluded, we argue that the submarine hydrothermal activity may be related either to the presence of magmas intruded into shallow crustal levels or remnants of the magmatic bodies responsible for the latest volcanism of the islands.

### 5.3. Fluids Versus Plio-Pleistocene Magmatic Activity

Here we discuss the geochemical features of the vented fluids within the geochemical framework of the Pontine magmatic rocks, with the aim of better constraining the origin of the vented fluids.

The magmatic activity of the western Pontine Archipelago developed during two main eruptive cycles. The first cycle occurred during the Pliocene (4.5–2.9 Ma [Cadoux *et al.*, 2005]) with the emplacement of subalkaline rhyolites (Pliocene rhyolites, PLIR) of high-K calcalkaline series (probably one of the last episodes of the circum Tyrrhenian calcalkaline volcanism). The second cycle developed during the Pleistocene with the extrusion of K-alkaline trachytes (Pleistocene trachytes, PLET) dated at about 1.0 Ma [Cadoux *et al.*, 2005] and considered as the first manifestations of the K-alkaline magmatism which successively developed southeastward in the eastern Pontine Islands and, more generally, in the Campanian Region (including the Ischia and Procida Islands and the Phlegrean fields-Vesuvius area [e.g., Beccaluva *et al.*, 1991]).

Due to the lack of poorly differentiated magmas among the volcanites of the two cycles, different petrogenetic processes have been suggested for their origin, including both crystal fractionation from mantle-derived basic magmas [Conte and Dolfi, 2002; Cadoux *et al.*, 2005; Conte *et al.*, 2016] and partial melting at crustal levels (i.e., anatexis [Paone, 2013]). The anatexis processes have been extensively considered for the Pliocene calcalkaline rhyolites, PLIR, due to their Sr-Nd isotope signatures, marking a stronger

involvement of crustal materials with respect to the Pleistocene trachytes PLET. However, based on major and trace element signatures, processes relating to upper crustal anatexis have been discarded by *Conte and Dolfi* [2002] and *Cadoux et al.* [2005] in favor of derivation from mantle-derived melts. *Paone* [2013] reconciles chemical and isotopic data by assuming that the Pliocene rhyolites were derived from the partial melting of mafic lower crust. Analyses from newly collected submarine lava samples [*Conte et al.*, 2016], including relatively undifferentiated rocks of the calcalkaline series (SAS, Submarine Andesite Samples), reinforce the hypothesis that the PLIR likely originated by the evolution of melts from a mantle source deeply contaminated by crustal components. This fits with the unusually high  $^{87}\text{Sr}/^{86}\text{Sr}$  (0.710422–0.710484) and low  $^{143}\text{Nd}/^{144}\text{Nd}$  (0.512208–0.512227) ratios of the SAS [*Conte et al.*, 2016], showing that the extremely radiogenic Sr and the nonradiogenic Nd isotopic values were a common feature of the parental melts and not related to shallow-level crustal assimilation.

In contrast, there is a general consensus in relating the PLET to fractional crystallization processes from a parental magma similar to the least evolved magma of the Campanian Volcanic District (e.g., Ventotene trachybasalt [*Fedele et al.*, 2003; *Paone*, 2013; *Conte et al.*, 2016]).

Figure 10 shows the  $^3\text{He}/^4\text{He}$ - $^{87}\text{Sr}/^{86}\text{Sr}$  relationship that appears to indicate binary mixing between two geochemically distinct crustal and mantle end-members. The mantle end-members are represented by MORB (Mid-Ocean Ridge Basalt) (although there is no evidence of a MORB-type mantle in the source region of the Tyrrhenian volcanic edifices [*Martelli et al.*, 2004]) and SCEM (Subcontinental European Mantle [*Dunai and Baur*, 1995]), as it is characterized by variable crustal contamination of the mantle wedge and as recognized within the Roman Comagmatic Province [*Martelli et al.*, 2004], the Campi Flegrei [*Pappalardo et al.*, 2002], Roccamonfina, and Vesuvius [*Paone*, 2004, 2006]. The adoption of a different mantle end-member, however, does not affect the meaning of the graph or of this discussion.

Most of the He and Sr isotopic data of Figure 10 refer to values measured on the same rock sample, whereas the samples from Ponza (Pliocene rhyolites, PLIR and Pleistocene trachyte, PLET) are plotted assuming that those rock types are releasing gases with the measured helium isotopic ratio. In particular, the comparison between the geochemistry of the fluid emissions and those of the Sr-isotope features of the Pliocene and Pleistocene volcanic products reported in Figure 10 highlights how the PLIR and PLET are located at different distances from the binary mantle-crust mixing lines. Taking into account the above mentioned consideration, three different scenarios for the isotopic ratios of helium and strontium can be proposed.

1. The source of the analyzed fluids is a magma similar to the Pliocene rhyolite (PLIR, grey mark) assumed to derive from partial melting of a mafic lower crust, according to *Paone* [2013]. In this case the corresponding isotopic composition ( $^{87}\text{Sr}/^{86}\text{Sr}$  and  $^3\text{He}/^4\text{He}$ ) would be representative of a mixture of volatiles from the hot mafic magma responsible for the partial melting of the lower crust (underplating) and volatiles released by the anatectic melt. However, the position of the PLIR grey mark far from the crust-mantle mixing curve indicates the nature of the source material that cannot be reproduced by a mixing of mantle-derived melts and crustal source.
2. The source of the analyzed fluids is a magma similar to the PLIR assumed to be originated by crystal fractionation of highly radiogenic SAS [*Conte et al.*, 2016]. In this case the helium isotopic composition (expressed as  $R/R_{\text{a}}$ ) of PLIR cannot attain the value of the analyzed fluids (reported in Figure 10), but rather it would approach that of its "parental" andesite, which should be close to mixing line 2 or even lower, considering its highly crustal-contaminated mantle source. Based on this hypothesis an origin of the analyzed fluids from magmas similar to those of the Pliocene cycle seems to be unlikely, due to the helium isotopic signature of the collected fluids. As a consequence it seems that the gases presently vented at the seafloor cannot be related to a PLIR-like magmatic source.
3. A third hypothesis is that the vented gases derive from a magma similar to the Pleistocene trachytes (PLET). In this case the measured helium and Sr isotopic ratios would be consistent. In fact, the high PLET Sr isotopic ratios, due to a small degree of crustal assimilation during evolution, yield a correct Sr isotopic ratio if the trachyte parental melt (i.e., the Ventotene trachybasalt studied by *D'Antonio et al.* [1999], AVT in Figure 10) is considered. Its Sr isotopic ratio plots (red mark in Figure 10) within the 2 and 5 binary mixing lines, close to the values of mafic products from the nearby volcanic areas (Ischia, Vesuvio, and Campi Flegrei).

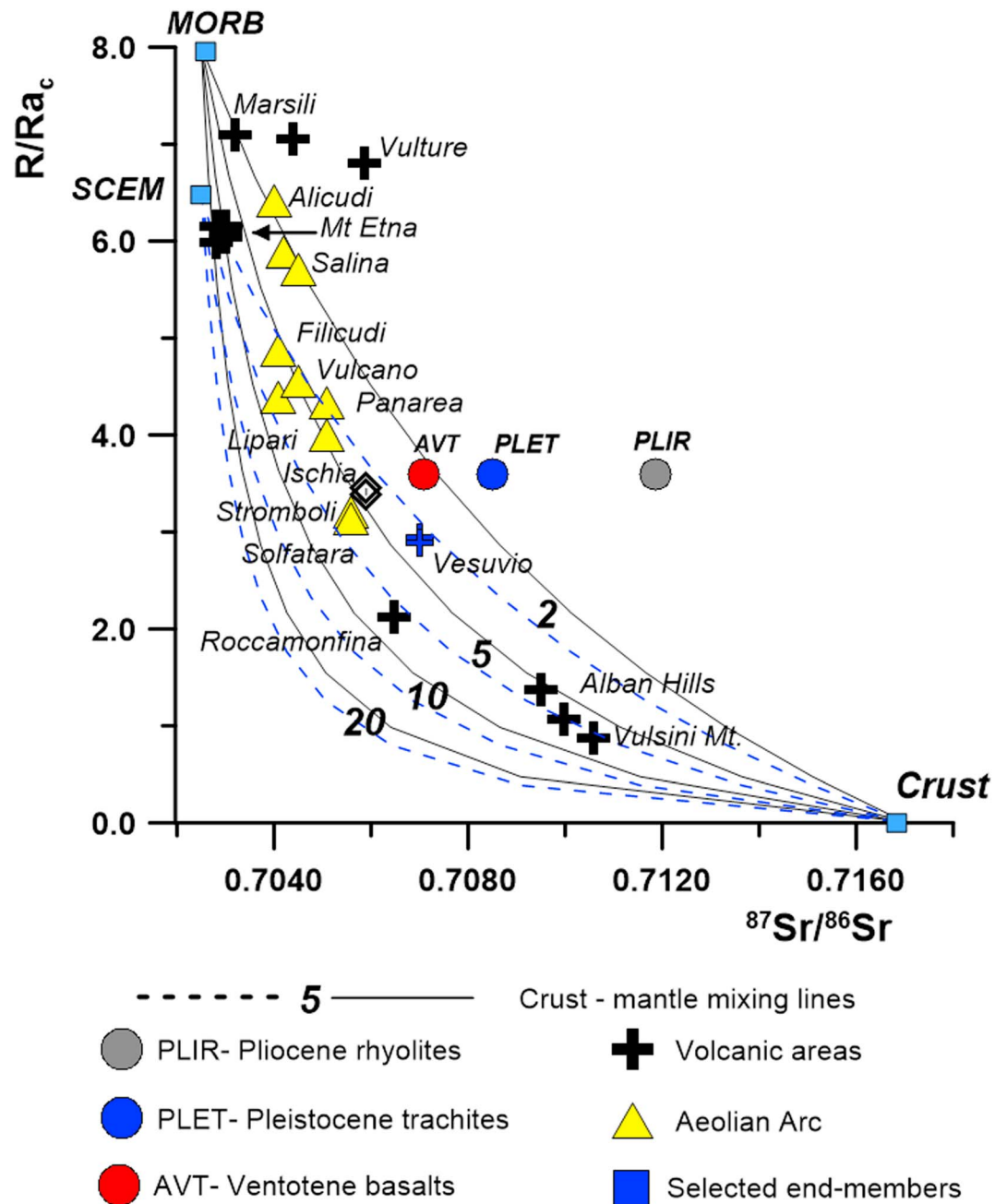


**Figure 10.** Plot of  $^{87}\text{Sr}/^{86}\text{Sr}$  versus  $R/Ra_c$  for solid and gaseous samples from the Tyrrhenian area. Binary mixing lines between MORB-like asthenosphere mantle and SCEM-type mantle (Subcontinental European Mantle [Dunai and Baur, 1995]) with a crustal end-member are shown as solid black lines for the former and blue dashed lines the latter. Numbers (2, 5, 10, and 20) indicate the  $k$  value [ $k = (\text{He}/\text{Sr})_{\text{crust}}/(\text{He}/\text{Sr})_{\text{mantle}}$ ] for each curve. Values for MORB and crust end-members:  $^3\text{He}/^4\text{He}_{\text{radiogenic}} = 0.01 \text{ Ra}$  [O'Nions and Oxburgh, 1988];  $^3\text{He}/^4\text{He}_{\text{MORB}} = 8 \text{ Ra}$  [Moreira and Kurz, 2001];  $^3\text{He}/^4\text{He}_{\text{asthenosphere}} = 0.7030$  [Marty et al., 1994].  $\text{He}_{\text{cont crust}} = 5 \times 10^{-5} \text{ cm}^3 \text{ STP/g}$  [Allegre et al., 1986/87];  $\text{He}_{\text{HIMU}} = 5 \times 10^{-7} \text{ cm}^3 \text{ STP/g}$  [Moreira and Kurz, 2001];  $\text{Sr}_{\text{cont crust}} = 333 \text{ ppm}$  [Wedepohl, 1995]; and  $\text{Sr}_{\text{MORB}} = 16.4 \text{ ppm}$  [Hilton et al., 1992]. Data after D'Antonio et al. [1999], Martelli et al. [2004], and Italiano et al. [2014b].

## 6. Conclusions

Based on morphological characteristics and the occurrence of areas characterized by active vents emitting hydrothermal-related fluids, the giant depressions, the cone-shaped morphologies, and the pockmarks

observed off Zannone Island represent various elements of an undocumented submarine hydrothermal field. The presence of these hydrothermal depressions highlights the occurrence of a wide area (roughly 60 km<sup>2</sup>) affected by geothermal activity, whose extent is likely controlled by tectonic structures of the Ponza-Zannone structural high and fed by hot volatiles of magmatic origin. This interpretation is supported by the geochemical features of the vented CO<sub>2</sub>-dominant gases, including helium isotopic ratios >3 Ra and the isotopic composition of carbon in CH<sub>4</sub> that indicates the late addition of thermogenic methane produced by equilibration processes inside an active geothermal system. The warm sea water temperature inside the depressions and the widespread anomalies of dissolved CO<sub>2</sub> further support the existence of a hydrothermal system off Zannone Island.

The thermal source feeding the hydrothermal system produces volatiles that may originate from residual magma batches, similar to the Pleistocene trachytes that were probably intruded in the shallow crustal levels and never erupted.

### Acknowledgments

We would like to thank all the officers, crew, and technicians of the R/V *Urania* and R/V *Maria Grazia* for their precious work. Part of the research was performed in the framework of the Flagship Project RITMARE (SP4-WP2-A1). The Associate Editor and two anonymous reviewers are gratefully acknowledged for their useful comments which helped us to improve the final version of the manuscript. L.M. has been supported through the Marie Curie Fellowship cofunded by the European Union under FP7-People cofunding of Regional, National, and International Programmes, GA 600407, and RITMARE Flagship Project. The data for this paper are available by contacting the corresponding author at [leonora.martorelli@igag.cnr.it](mailto:leonora.martorelli@igag.cnr.it).

### References

- Allegre, C. J., T. Staudacher, and P. Sarda (1986/87), Rare gas systematics: Formation of the atmosphere evolution and structure of the Earth's mantle, *Earth Planet. Sci. Lett.*, *81*, 127–150.
- Barberi, S., G. Borsi, F. Ferrara, and F. Innocenti (1967), Contributo alla conoscenza vulcanologica e magmatologia delle isole dell' Arcipelago Pontino, *Mem. Soc. Geol. Ital.*, *6*, 581–606.
- Beccaluva, L., P. Di Girolamo, and G. Serri (1991), Petrogenesis and tectonic setting of the Roman Volcanic Province, Italy, *Lithos*, *26*(3), 191–221.
- Cadoux, A., D. L. Pinti, C. Aznar, S. Chiesa, and P. Y. Gillot (2005), New chronological and geochemical constraints on the genesis and geological evolution of Ponza and Palmarola Volcanic Islands (Tyrrhenian Sea, Italy), *Lithos*, *81*, 121–151.
- Cavarretta, G., G. Gianelli, G. Scandiffio, and F. Tecce (1985), Evolution of the Latera geothermal system II: Metamorphic, hydrothermal mineral assemblages and fluid chemistry, *J. Volcanol. Geotherm. Res.*, *26*, 337–364.
- Conte, A. M., and D. Dolfi (2002), Petrological and geochemical characteristics of Plio-Pleistocene volcanic from Ponza Island (Tyrrhenian Sea, Italy), *Miner. Petrol.*, *74*(1), 75–94.
- Conte, A. M., C. Perinelli, G. Bianchini, C. Natale, E. Martorelli, and F. L. Chiocci (2016), New insights on the petrology of submarine volcanics from the Western Pontine Archipelago (Tyrrhenian Sea, Italy), *J. Volcanol. Geotherm. Res.*, doi:10.1016/j.jvolgeores.2016.08.005, in press.
- D'Antonio, M., L. Civetta, and P. Di Girolamo (1999), Mantle source heterogeneity in the Campanian Region (South Italy) as inferred from geochemical and isotopic features of mafic volcanic rocks with shoshonitic affinity, *Miner. Petrol.*, *67*, 163–192.
- De Rita, D., R. Funiello, D. Pantosti, F. Salvini, A. Sposato, and M. Velonà (1986), Geological and structural characteristics of the Pontine Islands (Italy) and implications with the evolution of the Tyrrhenian margin, *Mem. Soc. Geol. Ital.*, *36*(7), 55–65.
- Della Vedova, B., G. Pellis, J. P. Foucher, and J. P. Rehault (1984), Geothermal structure of the Tyrrhenian Sea, *Mar. Geol.*, *55*(3), 271–289.
- Dogliani, C., P. Harabaglia, S. Merlini, F. Mongelli, A. Peccerillo, and C. Piromallo (1999), Orogens and slabs vs. their direction of subduction, *Earth Sci. Rev.*, *45*, 167–208.
- Dunai, T. J., and H. Baur (1995), Helium, neon, and argon systematics of the European subcontinental mantle: Implications for its geochemical evolution, *Geochim. Cosmochim. Acta*, *59*(13), 2767–2783.
- Faccenna, C., C. Piromallo, A. Crespo-Blanc, L. Jolivet, and F. Rossetti (2004), Lateral slab deformation and the origin of the western Mediterranean arcs, *Tectonics*, *23*, TC1012, doi:10.1029/2002TC001488.
- Fedele, L., R. J. Bodnar, B. DeVivo, and R. Tracy (2003), Melt inclusion geochemistry and computer modeling of trachyte petrogenesis at Ponza, Italy, *Chem. Geol.*, *194*(1), 81–104.
- Fisher, A. T. (2004), Rates and patterns of fluid circulation, in *Hydrogeology of the Oceanic Lithosphere*, edited by E. E. Davis and H. Elderfield, pp. 339–377, Cambridge Univ. Press, Cambridge, U. K.
- Funiello, R., G. Mariotti, M. Parotto, M. Preite-Martinez, F. Tecce, R. Toneatti, and B. Turi (1979), Geology, mineralogy and stable isotope geochemistry of the Cesano geothermal field (Sabatini Mountains, Northern Latium, Italy), *Geothermics*, *8*, 55–73.
- Gay, A., M. Lopez, C. Berndt, and M. Sèrnanne (2007), Geological controls on focused fluid flow associated with seafloor seeps in the Lower Congo Basin, *Mar. Geol.*, *244*, 68–92.
- Graziani, S., S. E. Beaubien, S. Bigi, and S. Lombardi (2014), Spatial and temporal pCO<sub>2</sub> marine monitoring near Panarea Island (Italy) using multiple low-cost GasPro sensors, *Environ. Sci. Technol.*, *48*, 12,126–12,133, doi:10.1021/es500666u.
- Hannington, M. D., C. D. de Ronde, D. J. Cornell, and S. Petersen (2005), Sea-floor tectonics and submarine hydrothermal systems, in *Economic Geology 100th Anniversary Volume*, edited by J. W. Hedenquist et al., pp. 111–141, Soc. Econ. Geol., Littleton, Colo.
- Hawkesworth, C. J., and R. Vollmer (1979), Crustal contamination versus enriched mantle: <sup>143</sup>Nd/<sup>144</sup>Nd and <sup>87</sup>Sr/<sup>86</sup>Sr evidence from the Italian volcanoes, *Contrib. Mineral. Petrol.*, *69*, 151–165.
- Hilton, D. R., J. A. Hoogewerf, M. J. Van Bergen, and K. Hammerschmidt (1992), Mapping magma sources in the Sunda-Banda arcs, Indonesia: Constraints from helium isotopes, *Geochim. Cosmochim. Acta*, *56*, 851–859.
- Holocher, J., F. Peeters, W. Aeschbach-Hertig, M. Hofer, M. Brennwald, W. Kinzelbach, and R. Kipfer (2002), Experimental investigations on the formation of excess air in quasi-saturated porous media, *Geochim. Cosmochim. Acta*, *66*, 4103–4117.
- Ingrassia, M. (2016), Integrated bio-geological analysis of fluid related features offshore the Pontine Archipelago (central Tyrrhenian Sea, Italy) PhD thesis, 189 pp., Sapienza Univ., Rome.
- Ingrassia, M., E. Martorelli, A. Bosman, L. Macelloni, A. Sposato, and F. L. Chiocci (2015), The Zannone Giant Pockmark: First evidence of a giant complex seeping structure in shallow-water, central Mediterranean Sea, Italy, *Mar. Geol.*, *363*, 28–51, doi:10.1016/j.margeo.2015.02.005.
- Italiano, F. (2009b), Hydrothermal fluids vented at shallow depths at the Aeolian Islands: Relationships with volcanic and geothermal systems, *FOG Freiberg Online Geol.*, *22*, 55–60.
- Italiano, F., and P. M. Nuccio (1991), Geochemical investigations of submarine volcanic exhalations to the east of Panarea, Aeolian Islands, Italy, *J. Volcanol. Geotherm. Res.*, *46*(1), 125–141.

- Italiano, F., M. Martelli, G. Martinelli, and P. M. Nuccio (2000), Geochemical evidences of melt intrusions along lithospheric faults of Irpinian Apennines (Southern Italy): Geodynamic and seismogenetic implications, *J. Geophys. Res.*, *105*(B6), 13,569–13,578.
- Italiano, F., G. Martinelli, and P. Plescia (2008), CO<sub>2</sub> degassing over seismic areas: The role of mechanochemical production at the study case of Central Apennines, *Pure Appl. Geophys.*, *165*(1), 75–94.
- Italiano, F., P. Bonfanti, M. Ditta, R. Petrini, and F. Slejko (2009a), Helium and carbon isotopes in the dissolved gases of Friuli region (NE Italy): Geochemical evidence of CO<sub>2</sub> production and degassing over a seismically active area, *Chem. Geol.*, *266*, 76–85.
- Italiano, F., G. Yuce, I. T. Uysal, M. Gasparon, and G. Morelli (2014a), Insights into mantle-type volatiles contribution from dissolved gases in artesian waters of the Great Artesian Basin, Australia, *Chem. Geol.*, *378–379*, 75–88.
- Italiano, F., A. De Santis, P. Favali, M. L. Rainone, S. Rusi, and P. Signanini (2014b), The Marsili volcanic seamount (Southern Tyrrhenian Sea): A potential offshore geothermal resource, *Energies*, *7*, 4068–4086, doi:10.3390/en7074068.
- Judd, A. G., and M. Hovland (2007), *Seabed Fluid Flow: Impact on Geology, Biology and the Marine Environment*, Cambridge Univ. Press, Cambridge, U. K.
- Loreto, M. F., F. Pepe, R. De Ritis, A. M. Collura, V. Ferrante, F. Italiano, M. Sacchi, M. Speranza, and I. Tomini (2014), On the relationships between tectonics and volcanism in the offshore Capo Vaticano, SE Tyrrhenian Sea, during the Plio-Pleistocene indicators, *Rend. Online Soc. Geol. Ital.*, *31*(1), 85–98.
- Loreto, M. F., F. Italiano, D. Deponte, L. Facchin, and F. Zgur (2015), Mantle degassing on a near shore volcano, SE Tyrrhenian Sea, *Terra Nova*, *27*(3), 195–205.
- Lupton, J., et al. (2011), Active hydrothermal discharge on the submarine Aeolian Arc, *J. Geophys. Res.*, *116*, B02102, doi:10.1029/2010JB007738.
- Malinverno, A., and W. B. Ryan (1986), Extension in the Tyrrhenian Sea and shortening in the Apennines as result of arc migration driven by sinking of the lithosphere, *Tectonics*, *5*(2), 227–245, doi:10.1029/TC005i002p00227.
- Marani, M., and N. Zitellini (1986), Rift structures and wrench tectonics along the continental slope between Civitavecchia and C. Circeo, *Mem. Soc. Geol. Ital.*, *35*, 453–457.
- Marani, M., M. Taviani, F. Trincardi, A. Argnani, A. M. Borsetti, and N. Zitellini (1986), Pleistocene progradation and postglacial events of the NE Tyrrhenian continental shelf between the Tiber river delta and Capo Circeo, *Mem. Soc. Geol. Ital.*, *36*, 67–89.
- Martelli, M., P. M. Nuccio, F. M. Stuart, R. Burgess, R. M. Ellam, and F. Italiano (2004), Helium-strontium isotope constraints on mantle evolution beneath the Roman Comagmatic Province, (Italy), *Earth Planet. Sci. Lett.*, *224*, 295–308.
- Marty, B., T. Trull, P. Lussiez, I. Basile, and J. C. Tanguy (1994), He, Ar, O, Sr and Nd isotope constraints on the origin and evolution of Mount Etna magmatism, *Earth Planet. Sci. Lett.*, *126*, 23–39.
- Maugeri, T. L., G. Bianconi, F. Canganella, R. Danovaro, C. Gugliandolo, F. Italiano, V. Lentini, E. Manini, and B. Nicolaus (2010), Shallow hydrothermal vents in the southern Tyrrhenian Sea, *Chem. Ecol.*, *26*(S1), 285–298.
- Minissale, A. (2004), Origin, transport and discharge of CO<sub>2</sub> in central Italy, *Earth Sci. Rev.*, *66*(1), 89–141.
- Monecke, T., S. Petersen, M. D. Hannington, M. Anzidei, A. Esposito, G. Giordano, D. G. Schönberg, N. Augustin, B. Melchert, and M. Hocking (2012), Explosion craters associated with shallow submarine gas venting off Panarea Island, Italy, *Bull. Volcanol.*, *74*(9), 1937–1944.
- Moreira, M., and M. D. Kurz (2001), Subducted oceanic lithosphere and the origin of the ‘high I’ basalt helium isotopic signature, *Earth Planet. Sci. Lett.*, *189*, 49–57.
- O’Nions, R. K., and E. R. Oxburgh (1988), Helium, volatile fluxes and the development of continental crust, *Earth Planet. Sci. Lett.*, *90*, 331–347.
- Paone, A. (2004), Evidence of crustal contamination, sediment, and fluid components in the Campanian volcanic rocks, *J. Volcanol. Geotherm. Res.*, *138*(1), 1–26.
- Paone, A. (2006), The geochemical evolution of the Mt. Somma-Vesuvius volcano, *Miner. Petrol.*, *87*(1–2), 53–80.
- Paone, A. (2013), Petrogenesis of trachyte and rhyolite magmas on Ponza Island (Italy) and its relationship to the Campanian magmatism, *J. Volcanol. Geotherm. Res.*, *267*, 15–29.
- Pappalardo, L., M. Piochi, M. d’Antonio, L. Civetta, and R. Petrini (2002), Evidence for multi-stage magmatic evolution during the past 60 kyr at Campi Flegrei (Italy) deduced from Sr, Nd and Pb isotope data, *J. Petrol.*, *43*(8), 1415–1434.
- Passaro, S., et al. (2014), First hydroacoustic evidence of marine, active fluid vents in the Naples Bay continental shelf (Southern Italy), *J. Volcanol. Geotherm. Res.*, *285*, 29–35.
- Passaro, S., et al. (2016), Seafloor doming driven by degassing processes unveils sprouting volcanism in coastal areas, *Sci. Rep.*, *6*, 22448, doi:10.1038/srep22448.
- Peccerillo, A. (2003), Plio-Quaternary magmatism in Italy, *Episodes*, *26*(3), 222–226.
- Pilcher, R., and J. Argent (2007), Mega-pockmarks and linear pockmark trains on the West African continental margin, *Mar. Geol.*, *244*, 15–32.
- Rovere, M., F. Gamberi, A. Mercorella, H. Rashed, A. Gallerani, E. Leidi, M. Marani, V. Funari, and G. A. Pini (2014), Venting and seepage systems associated with mud volcanoes and mud diapirs in the southern Tyrrhenian Sea, *Mar. Geol.*, *347*, 153–171.
- Sano, Y., and H. Wakita (1988), Precise measurement of helium isotopes in terrestrial gases, *Bull. Chem. Soc. Jpn.*, *61*(4), 1153–1157.
- Sartori, R. (2003), The Tyrrhenian backarc basin and subduction of the ionian lithosphere, *Episodes*, *26*, 217–221.
- Spallanzani, L. (1792), *Viaggi alle Due Sicilie e in alcune parti dell’Appennino*, vol. 6, pp. 1795–1798, B. Comini, Pavia.
- Stüben, D., P. Sedwick, and P. Colantoni (1996), Geochemistry of submarine warm springs in the limestone cavern of Grotta Azzurra, Capo Palinuro, Italy: Evidence for mixing-zone dolomitisation, *Chem. Geol.*, *131*(1), 113–125.
- Suess, E. (2014), Marine cold seeps and their manifestations: Geological control, biogeochemical criteria and environmental conditions, *Int. J. Earth Sci.*, *103*(7), 1889–1916.
- Tricoli, G. (1855), *Monografia per le Isole del Gruppo Ponziato*, vol. 4, pp. 1–437, Stamperia Vico S. Marcellino, Napoli.
- Walker, S. L., S. Carey, K. L. Bell, E. T. Baker, K. Faure, M. Rosi, M. Marani, and P. Nomikou (2012), Near-bottom water column anomalies associated with active hydrothermal venting at Aeolian arc volcanoes, Tyrrhenian Sea, Italy paper presented at AGU Fall Meeting Abstracts, vol. 1, p. 1906.
- Wedepohl, K. H. (1995), The composition of the continental crust, *Geochim. Cosmochim. Acta*, *59*, 1217–1231.
- Zitellini, N., M. Marani, and A. Borsetti (1984), Post-orogenic tectonic evolution of Palmarola and Ventotene basins (Pontine Archipelago), *Mem. Soc. Geol. Ital.*, *27*, 121–131.